FINITE ELEMENT ANALYSIS OF ACOUSTIC WAVE TRANSVERSE TO LONGITUDINAL COUPLING DURING TRANSVERSE COMBUSTION INSTABILITY

A Thesis
Presented to
The Academic Faculty

by

Jordan M. Blimbaum

In Partial Fulfillment
of the Requirements for the Degree
Master of Science in the
School of Mechanical Engineering

Georgia Institute of Technology
August 2012

FINITE ELEMENT ANALYSIS OF ACOUSTIC WAVE TRANSVERSE TO LONGITUDINAL COUPLING DURING TRANSVERSE COMBUSTION INSTABILITY

Approved by:

Dr. Tim Lieuwen, Advisor
School of Aerospace Engineering
Georgia Institute of Technology

Dr. Michael Leamy
School of Mechanical Engineering
Georgia Institute of Technology

Dr. Lakshmi Sankar
School of Aerospace Engineering
Georgia Institute of Technology

Date Approved: 05/18/12

ACKNOWLEDGEMENTS

Thank you,

Professor Tim Lieuwen

For your enthusiasm and insight

Friends and Family

For your continual support and understanding

My colleagues at the Combustion Laboratory and ISAE-ENSMA

For your patience and friendship

The brothers of Chi Alpha Delta

For your humor and encouragement

The US Department of Energy

For funding this worthwhile and exciting project

TABLE OF CONTENTS

LIST OF TABLES

Page

LIST OF FIGURES

LIST OF SYMBOLS AND ABBREVIATIONS

A	Rightward traveling wave amplitude
a	Nozzle dimension
B	Rightward traveling wave amplitude
c	Speed of sound
D	Nozzle dimension
F_{TL}	Transverse-to-Longitudinal flame transfer function
h	Nozzle dimension
IP	In-phase
k	Wavenumber
L_O	Effective length
L	Nozzle dimension
n	Directional factor
OP	Out-of-phase
p'	Pressure fluctuation
$\overline{p}'$	Spatially averaged pressure fluctuation
p_i'	Incident pressure fluctuation
$p_{\max}$	Maximum pressure
p_r'	Reflected pressure fluctuation
p_t'	Transmitted pressure
$\dot{q}$	Unsteady heat release
R	Fillet radius
r_i	Inner radius

r_o	Outer radius
R_Z	Impedance Ratio
S	Nozzle dimension
t	Time
u'	Velocity fluctuation
u'_x	Transverse velocity fluctuation
$\overline{u}'_x$	Spatially averaged transverse velocity fluctuation
u'_z	Axial (longitudinal) velocity fluctuation
$\overline{u}'_z$	Spatially averaged axial velocity fluctuation
x	Transverse coordinate
y	Spatial coordinate
z	Axial (longitudinal) coordinate
Z_b	1-D branch impedance
Z_i	Applied Impedance
Z_O	Swirler Impedance
Z_{tr}	Transmitted Impedance
Λ	Acoustic mode
λ	Wavelength
ρ	Density
ω	Angular frequency

SUMMARY

Velocity-coupled combustion instability is a major issue facing lean combustor design in modern gas turbine applications. In this study, we analyze the complex acoustic field excited by a transverse acoustic mode in an annular combustor. This work is motivated by the need to understand the various velocity disturbance mechanisms present in the flame region during a transverse instability event. Recent simulation and experimental studies have shown that much of the flame response during these transverse instabilities may be due to the longitudinal motion induced by the fluctuating pressure field above the nozzles. This transverse to longitudinal coupling has been discussed in previous work, but in this work it is given a robust acoustic treatment via computational methods in order to verify the mechanisms by which these two motions couple.

We will provide an in-depth discussion of this coupling mechanism and propose a parameter, R_Z, also referred to as the Impedance Ratio, in order to compare the pressure/velocity relationship at the nozzle outlet to quasi one-dimensional theoretical acoustic approximations. A three-dimensional inviscid simulation was developed to simulate transversely propagating acoustic pressure waves, based on an earlier experiment designed to measure these effects. Modifications to this geometry have been made to account for lack of viscosity in the pure acoustic simulation and are discussed.

Results from this study show that transverse acoustic pressure excites significant axial motion in and around the nozzle over a large range of frequencies. Furthermore, the development of R_Z offers a defined physical parameter through which to reference this important velocity-coupled instability mechanism. Therefore, this study offers an in-

depth and quantifiable understanding of the instability mechanism caused by transversely propagating acoustic waves across a combustor inlet, which can be applied to greatly improve annular combustor design in future low-emissions gas turbine engines.

CHAPTER 1

INTRODUCTION

Emissions regulations, reliability, and fuel costs are significant factors that drive combustion innovation. Combustion instabilities have arisen as one of the most critical problems facing development of robust, low emissions combustors for both power generation and aviation applications [1]. These instabilities can arise due to interactions between heat release and local flow perturbations. When these heat release oscillations are in-phase with the acoustic pressure oscillations, the flame adds energy to the acoustic field [2]. The instantaneous heat release rate of the flame is sensitive to several potentially oscillatory quantities, such as velocity and fuel/air ratio, and much work has been done to understand these mechanisms in combustion systems [3-8]. This study focuses specifically on transverse oscillations in combustion chambers, which have been historically problematic in rockets [9-12] and jet engine afterburners [13-15]. In addition, they appear in gas turbines in both annular and can combustion chambers [16-22].

In order to motivate the approach taken in this study, it is useful to consider in more detail a typical arrangement of annular combustor systems and transverse instabilities in these systems. A simplified schematic of such a system is shown in Figure 1. It illustrates an annular ring around which regularly spaced nozzles are placed. Air from the compressor exits these nozzles and flows in the axial flow direction. These nozzles have their own acoustic characteristics, associated with distributed inertia/compressibility in the flow passage, and the inertia and resistivity of the swirlers [18]. For systems with sufficient wave transmission through the swirler, the upstream

acoustic characteristics also come into play, such as the compressibility of the compressor discharge plenum.

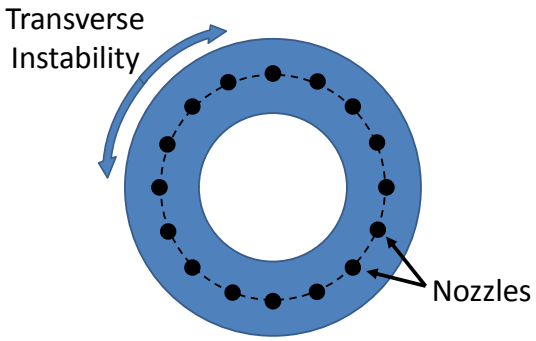

Figure 1: Simple schematic of an annular combustor

Having discussed the geometry, next consider the transverse modes in these systems. These modes can consist of standing and traveling waves in the azimuthal direction, and standing waves in the radial direction. In many cases, nozzles could be situated at any point in the standing wave field, because nozzles are distributed around the combustor. For example, a nozzle situated near the velocity node and another near the pressure node experience significantly different disturbance fields, and possibly different flame excitation physics. Moreover, these disturbance wavelengths could be quite long relative to the nozzle dimension in the case of annular modes, or on the same order of the wavelength for radial modes. In many cases, the oscillations in the azimuthal direction are closely approximated by traveling waves [18]. In this case, the flame response would vary significantly in time as the wave spins around the combustion chamber.

Recent work has shown that several paths exist in which a transverse mode may excite a flame [23-26]. As shown in Figure 2, transverse modes can directly excite the flame, they can excite hydrodynamic flow instabilities, and they can also lead to axial acoustic flow oscillations in the nozzle. Recent measurements and simulations have

suggested that these axial oscillations may be the dominant source of flame excitation during a transverse instability [23, 27, 28]. These axial acoustic oscillations are a wave diffraction effect, as the dominantly transverse mode leads to an oscillatory pressure field across the nozzle. This oscillatory pressure field induces axial flow oscillations, referred to as "injector coupling" in the rocket literature [29, 30].

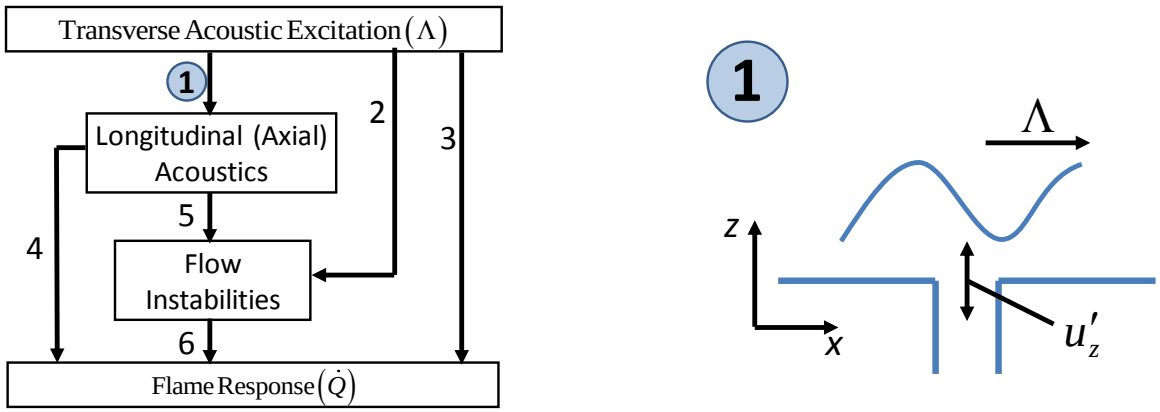

Figure 2: Pathways for velocity coupled combustion instabilities.

This study particularly focuses on transverse to axial acoustic coupling processes, path 1, in Figure 2. This is done by performing three-dimensional acoustic simulations for a non-flowing, inviscid, non-reacting environment using COMSOL Multiphysics [31]. As such, this analysis is useful for studying the disturbance field away from the boundary layers, where shear induced instabilities may be dominant, and for low Mach number flows.

The rest of this thesis is organized in the following manner. First, the model framework is presented. An important complication associated with an inviscid model arises from the infinite velocity fields that appear at sharp corners. In a viscous flow, this singularity is eliminated by vorticity production. This singularity inhibits convergence as the grid is refined. We discuss this issue, the geometry modifications, and the gridding work undertaken to ensure a grid-independent solution. Then, we present the basic

characteristics of the pressure and three-dimensional acoustic velocity field in the vicinity of the nozzle. Results are shown for cases where the nozzle is located at a pressure and velocity node, as well as when it is subjected to a traveling wave. Finally, we show that the upstream impedance of the nozzle has important influences on the axial acoustic velocity, and show how the impedance translation theorem can be used to provide a useful interpretation of the bulk axial disturbance field in several cases.

CHAPTER 2

MODEL FRAMEWORK

This chapter details the development of the finite element acoustic model used to generate results detailed in later chapters. Here we cover the motivation for the model, the development of the dimensions and boundary conditions, how singularities were addressed, and the meshing work undertaken to ensure that the results obtained are useful and accurate.

Motivation for Development

The physical domain for the finite element model was selected to resemble an existing experimental facility from which related data was obtained, as shown in Figure 3, below.

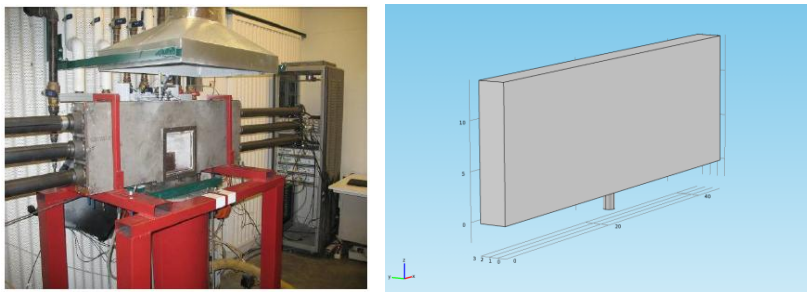

Figure 3: Experimental setup (left) and computational model (right).

The data obtained from the experimental setup showed that axial velocity is excited by transverse acoustic modes in the nozzle region of an annular combustor [32]. This study, aimed at understanding how transverse acoustics and axial velocity couple, generated much knowledge and curiosity about this velocity coupled instability.

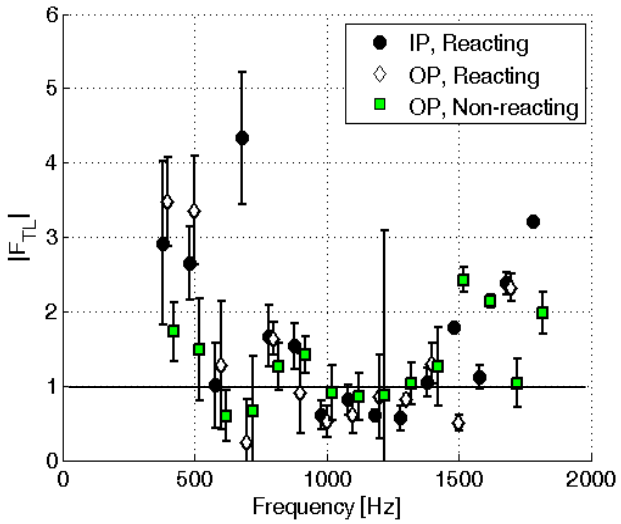

Figure 4: Existing data illustrating evidence of transverse to longitudinal velocity coupled combustion instability [32].

Figure 4 displays experimental results for the transverse-to-longitudinal transfer function, F_{TL}, described by path 1 in Figure 2. IP and OP refer to in-phase and out-of-phase forcing configurations, which are described in detail later in this chapter. Unfortunately, it is hard to see clear trends in the experimental data due to many highly coupled flow and vortical mechanisms. Therefore, it is desired to isolate the transverse to longitudinal coupling mechanism using a non-reacting, no-flow, inviscid and purely acoustic simulation.

Finite Element Model

COMSOL Multiphysics (version 4.2) was used to model, mesh, and analyze this system, shown in Figure 5. The physical domain is 114.3 centimeters in length, 35.6 centimeters in height and 7.6 centimeters in depth. A nozzle section connects into the center of the box as illustrated in Figure 5, which has an outer diameter of 3.175 cm and inner diameter of 2.18 cm, and extends 5.08 cm from the bottom of the combustion chamber. The gas temperature is held uniformly at 298 K everywhere.

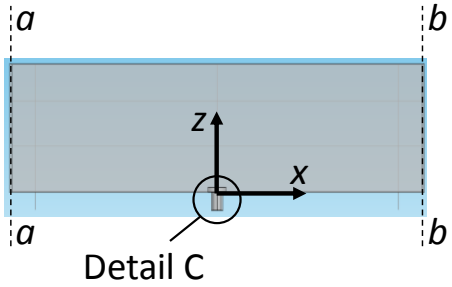

Figure 5: Schematic showing simulation domain and coordinate system.

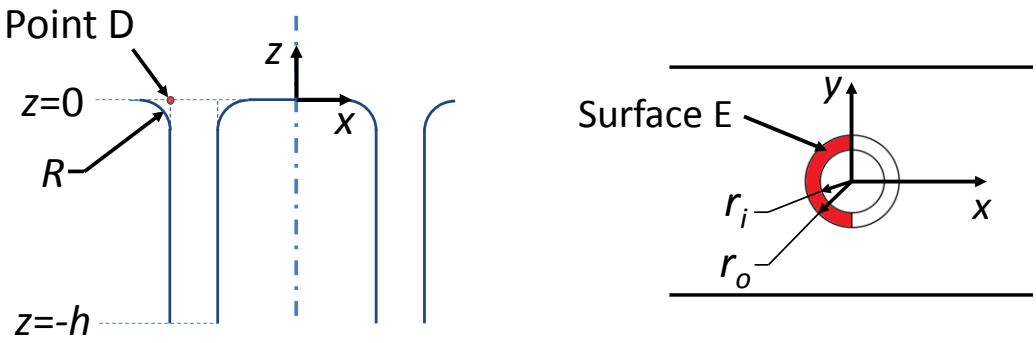

Figure 6: Detail C from Figure 5 showing centerbody and annulus, as well as fillet.

Since evanescent multi-dimensional disturbances are expected at the nozzle-combustor interface, the nozzle length, *h*, was chosen in order to ensure that the disturbance field has reverted to a nearly one-dimensional field at the opposite end of the nozzle, *z*=-*h*. This choice of *h*, coupled with the approach described later to specify the impedance at *z*=-*h*, eliminates sensitivity of these results to *h*.

Boundary Conditions

Forcing is employed by applying a spatially uniform pressure disturbance on the opposing faces of the chamber, shown as walls *a*-*a* and *b*-*b* in Figure 5. Three different velocity forcing fields were used, and are referred to as "in-phase", "out-of-phase", and "travelling wave" scenarios. The first two disturbance fields lead to standing wave fields in the system, where the combustor centerline is nominally a pressure anti-node and node, respectively. The velocity field exhibits a node and antinode, respectively. In the

third forcing scenario, an anechoic boundary is applied to the right side of the domain. In the absence of the nozzle, the acoustic field is one-dimensional and the three forcing scenarios display the magnitude profiles shown in Figure 7.

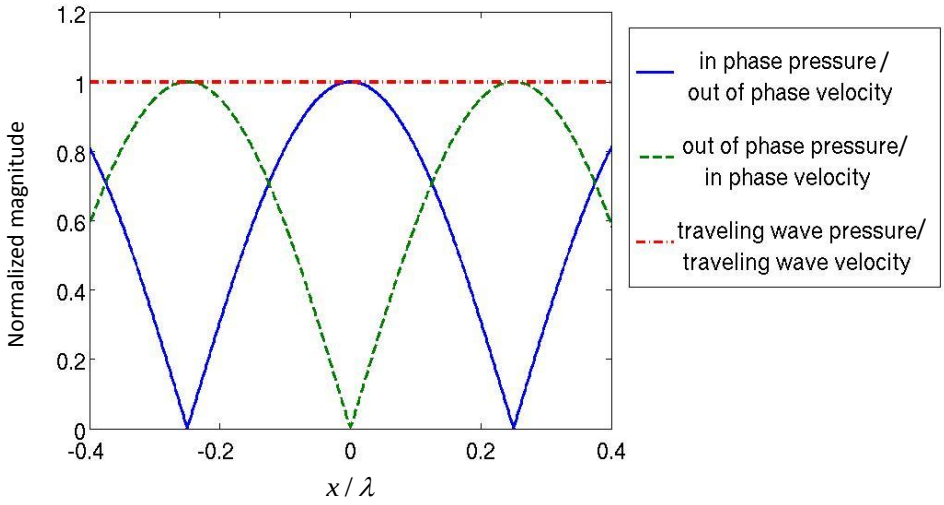

Figure 7: Acoustic pressure and velocity fields for three different forcing cases that occur in the absence of the side branch.

A spatially uniform impedance boundary condition, Z_0, is applied at the lower end of the nozzle section, $z=-h$. As noted above, the acoustic field reverts to a one-dimensional field at this end of the nozzle section, because the forcing frequency remains well below the transverse mode cutoff frequency for all frequencies considered in this study. We can then determine Z_0 by solving a one-dimentional acoustics translation problem using generic impedance boundary conditions. To do so, it is important to note that COMSOL uses the following convention [33]:

$$e^{i\omega t} \tag{1}$$

$$p' = Ae^{-ikx} + Be^{ikx} \tag{2}$$

We calculate velocity using the one-dimensional Euler equation:

$$u' = \frac{-1}{\rho c}\left[-Ae^{-ikx} + Be^{ikx}\right] \tag{3}$$

Using impedance boundary conditions at each end of the nozzle:

$$Z_0 = \frac{p'(x=0)}{u'(x=0)} \tag{4}$$

$$Z_{tr} = \frac{p'(x=h)}{u'(x=h)} \tag{5}$$

Note that for this nozzle geometry, $z = (x-h)$. Once the acoustic field is radially uniform in the nozzle, the relationship between the axial velocity and pressure in the nozzle is uniquely related to the nozzle impedance through the impedance translation theorem [34]:

$$\frac{Z_{tr}(z)}{\rho c} = -\left[\frac{\left(-\frac{Z_o}{\rho c}-1\right)e^{-ik(z+h)} + (-\frac{Z_o}{\rho c}+1)e^{ik(z+h)}}{\left(\frac{Z_o}{\rho c}+1\right)e^{-ik(z+h)} + (-\frac{Z_o}{\rho c}+1)e^{ik(z+h)}}\right] \tag{6}$$

For the results in this study, we chose Z_0 values such that $Z_{tr}(z=0)$ approximates pressure release, anechoic, and rigid boundary conditions by using $Z_{tr}/\rho c$ values of 0.01, 1, and 100, respectively. For this reason, a different Z_0 value is used at each frequency in order to maintain a fixed Z_{tr}.

It is also important to note that in COMSOL, the equation for applied impedance *(Z_o=Z_i)* is given by [33]:

$$-n\left(\frac{1}{-\rho c}\left(\nabla p_t' - q\right)\right) = -p_t' \frac{i\omega}{Z_i} \tag{7}$$

Therefore, Z_0 is highly directional. When Z is applied in the positive direction, Z_0 must be entered as negative, in order to allow a positive pressure to exit the interface. This is the case at the bottom of the nozzle.

Addressing Singularities

We next discuss the treatment of the nozzle-combustor interface geometry. Because singularities occur at sharp corners for inviscid flows, special care is required at the inside and outside corners of the annulus to insure that the simulated results are grid-independent. Singularities are avoided by adding a fillet radius, *R*, to the corners, as shown in Figure 6. While the fillets eliminate the singularities, they also introduce a new parameter, as the velocity field in the vicinity of these features becomes a function of *R*. To illustrate, Figure 8 shows the dependence of the axial velocity at location D indicated in Figure 6 upon fillet radius for the in-phase forcing case. For reference, a $1/\sqrt{R}$ line is also indicated in the figure, representing the theoretical result for a two-dimensional corner [34]. All results shown following this radius study are simulated using a radius of 0.02D, or 0.635 mm, which is indicated by the vertical dashed lines in Figure 8 through Figure 13. Reasons for choosing this radius will be discussed in the following sections.

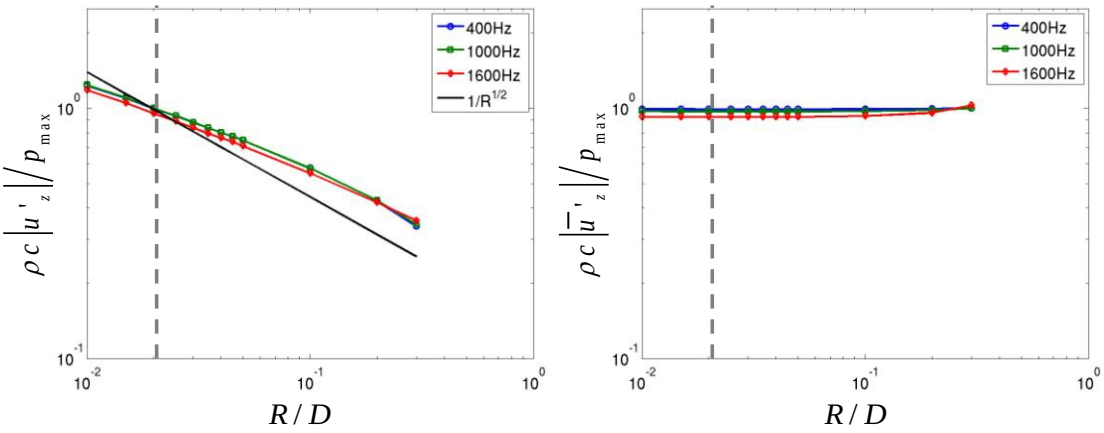

Figure 8: Dependence of axial velocity at point D in Figure 6 (left) and spatially averaged over surface E in Figure 6 (right) upon fillet radius at three frequencies, for in-phase forcing with $Z_{tr}/\rho c = 1$. The vertical dashed line indicates the fillet radius used for the results presented in this thesis.

Figure 8 on the right shows the average axial velocity at the nozzle-combustor junction, calculated on the top half annulus of the nozzle, shown in Figure 6, as

$$\overline{u'_z} = \frac{2}{\pi\left(r_o^{\,2} - r_i^{\,2}\right)} \int_0^{\pi} \int_{r_i - R}^{r_o + R} u'_z\left(r,\theta\right) \cdot r\,dr\,d\theta \tag{8}$$

This result shows that while the local velocity exhibits a significant dependence on *R* near the fillet, the spatially averaged axial velocity results are almost independent of radius. It is important to point out the steps taken to define the normalizing area used in equation (8). In the fillet region, the volume flow rate remains virtually constant as *z* varies from *z*=0 to -*R*. However, the averaging surface area does not remain constant. For this reason, the averaged axial velocity does vary with *z*, and similarly varies at *z*=0 with fillet radius. This effect is nothing more than a reflection of the dependence of nozzle outlet area at *z*=0 on *R*. In order to account for this geometry effect, we rescale the average axial velocity by the area ratio at *z*=0 and *z*=-*R*, and arrive at the formula shown in equation (8).

However, the total pressure above the nozzle does not remain constant as *z* varies from 0 to -*R*, since pressure is defined by a constant force divided by the changing area. Therefore, it is not necessary to multiply pressure by an area ratio. This gives equation (9) for pressure as:

$$\overline{p'} = \frac{2}{\pi\left(\left(r_o + R\right)^2 - \left(r_i - R\right)^2\right)} \int_0^{\pi} \int_{r_i - R}^{r_o + R} p'\left(r, \theta\right) \cdot r dr d\theta \tag{9}$$

Because transverse velocity is calculated directly from pressure through equation (3), the transverse velocity component also does not require manipulation by an area ratio.

$$\overline{u_x'} = \frac{2}{\pi\left(\left(r_o + R\right)^2 - \left(r_i - R\right)^2\right)} \int_0^{\pi} \int_{r_i - R}^{r_o + R} p'\left(r, \theta\right) \cdot r dr d\theta \tag{10}$$

The transverse velocity dependence on fillet radius for the in-phase forcing case is shown in Figure 9 below. Note that the transverse velocity follows the same trends that were observed axially.

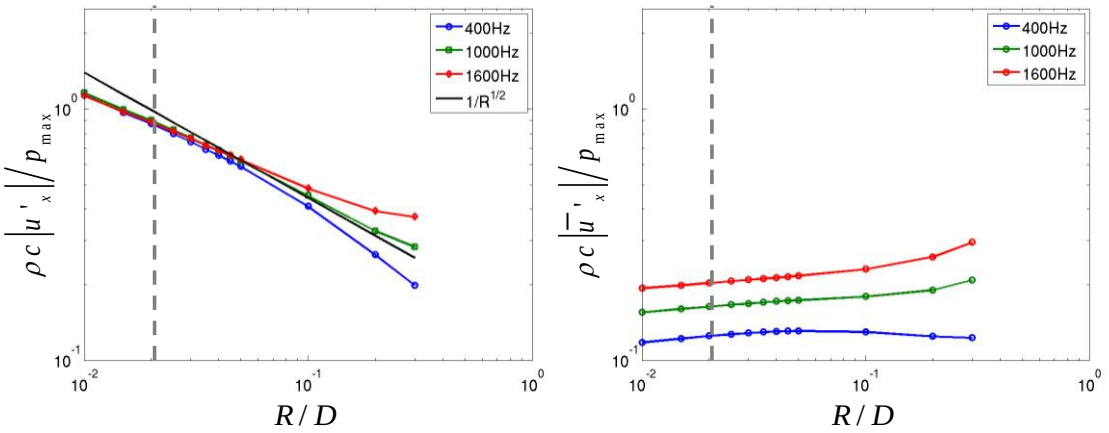

Figure 9: Dependence of transverse velocity at point D in Figure 6 (left) and spatially averaged over surface E in Figure 6 (right) upon fillet radius at three frequencies, for in-phase forcing with $Z_{tr}/\rho c = 1$.

The same radius study for the out-of-phase standing wave scenario describes similar results, shown in Figure 10 and Figure 11.

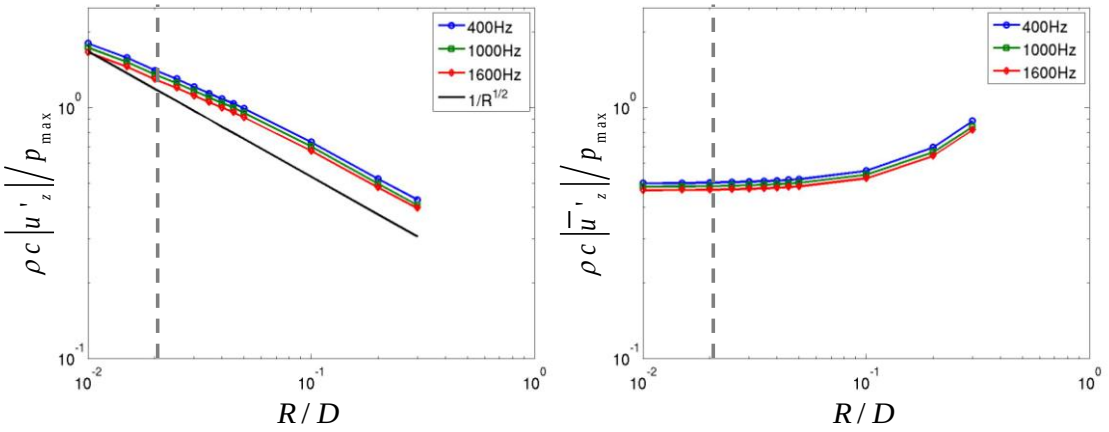

Figure 10: Dependence of axial velocity at point D in Figure 6 (left) and spatially averaged over surface E in Figure 6 (right) upon fillet radius at three frequencies, for out-of-phase forcing with an anechoic nozzle.

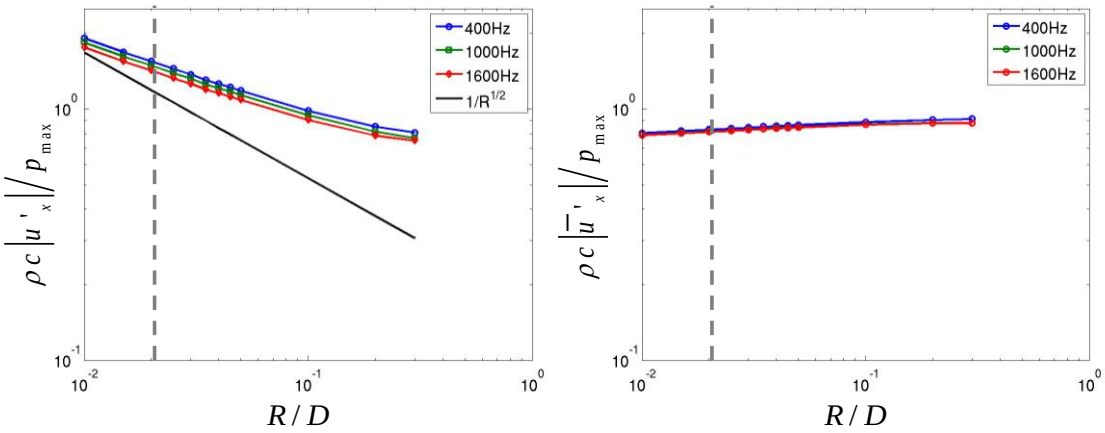

Figure 11: Dependence of transverse velocity at point D in Figure 6 (left) and spatially averaged over surface E in Figure 6 (right) upon fillet radius at three frequencies, for out-of-phase forcing with an anechoic nozzle.

Interestingly, while the traveling wave scenario seems to follow the theoretical approximation at a corner when observing axial velocity, this is not necessarily true for transverse velocity. It will be shown in later chapters that the traveling wave case behaves much differently than the standing wave cases, so following this singularity approximation may not be expected in this case. However, by applying the area ratio as described above, Figure 12 and Figure 13 show that both velocities approach acceptable results at small radii.

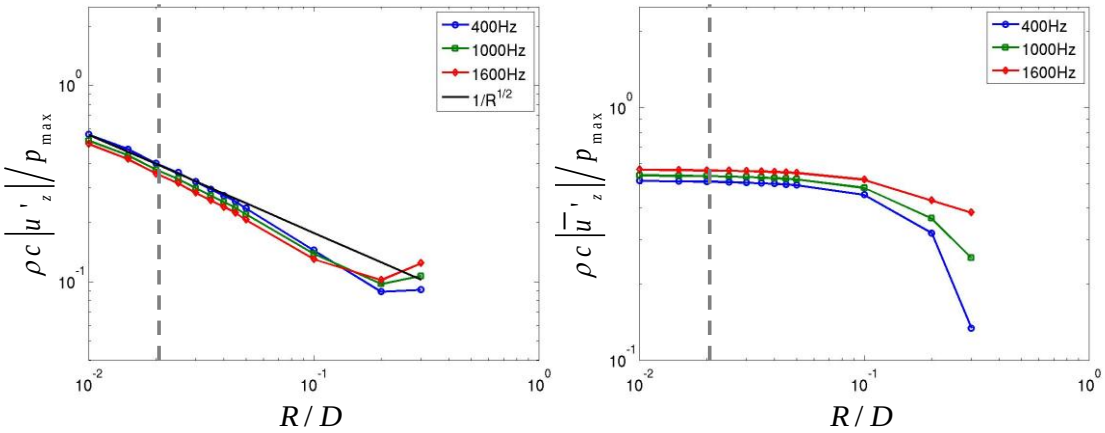

Figure 12: Dependence of axial velocity at point D in Figure 6 (left) and spatially averaged over surface E in Figure 6 (right) upon fillet radius at three frequencies, for a traveling wave with an anechoic nozzle.

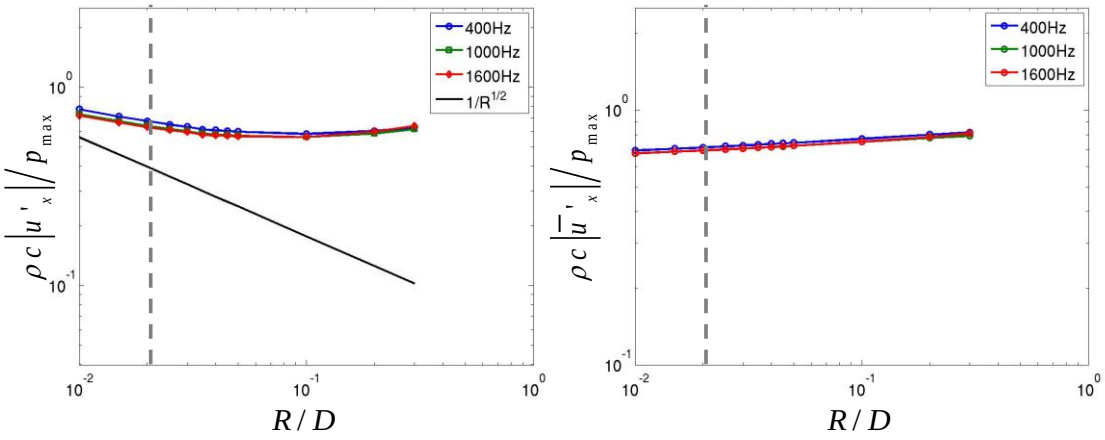

Figure 13: Dependence of transverse velocity at point D in Figure 6 (left) and spatially averaged over surface E in Figure 6 (right) upon fillet radius at three frequencies, for a traveling wave with an anechoic nozzle.

While eliminating the singularity, the fillet does require care in meshing. As the fillet radius near the inlet is decreased, the mesh size there must also decrease. However, drastically decreasing the size of the mesh in a fixed location causes a high contrast in local mesh density, which has a negative impact on the finite element mesh accuracy.

Mesh Development

In order to ensure mesh independence, it was desired to design multiple meshes to ensure that simulated results are independent of the mesh geometry. Since results near the nozzle-combustor junction are dependent on radius size, the main design factor when creating the mesh is to insure that the mesh size near the inlet is small enough to fit at least five mesh elements along the radius arc.

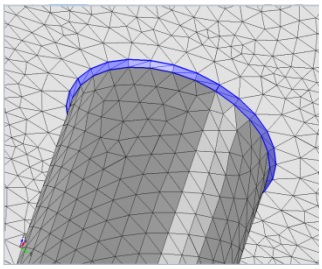

Figure 14: Fillet radius exhibiting insufficient meshing.

Three meshes were compared and are explained here:

Mesh 1

The inner and outer fillet radii were mapped so that the largest element length was at most equal to *R/3* on the radius face. The majority of the large combustor box was mapped with 0.5" square elements. At the time it was felt that square elements were the most efficient mesh scheme for traveling acoustic waves. Since the mesh is so fine near the inlet, growth boxes were created so that the mesh could easily transition from fine elements near the inlet to courser elements everywhere else. Interior cylindrical boundaries were also included inside the transition boxes to allow the cylindrical mesh from the inlet to easily transition to the rectangular geometry in the rest of the combustor. Free tetrahedral meshes were used for unmapped portions, but the element growth rate was restricted to 1.2 so as not to allow the elements to grow too rapidly away from the inlet, in order to preserve mesh quality. The resulting mesh included 741,865 elements, and exhibited a minimum mesh quality on the *x*-*z* plane greater than 0.2, which was a great improvement over meshes used previously for this geometry.

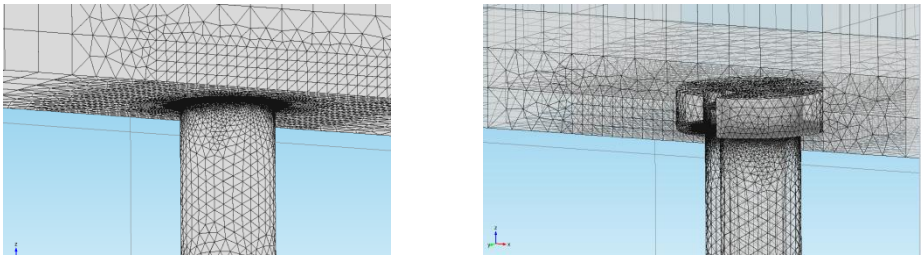

Figure 15: Mesh 1.

Mesh 2

From Mesh 1, the lowest mesh quality was observed at the boundaries between the mapped and tetrahedral meshes. Some of these boundaries were very near the fillet

radius, so Mesh 2 was designed to pull this low mesh quality away from the nozzle inlet by generating a mapped mesh section in neighboring regions, as shown in Figure 16 below. This change greatly improved clarity of results on this surface but also generated a large amount of elements in the nozzle region, so the element size everywhere else in the model had to be increased. It was found that COMSOL generally ran out of memory for computation after breaching the 1,000,000 element limit. Also, the *R=0.02D* radius size was no longer possible due to mesh size constraints, so an *R=0.025D* radius was used. The resulting mesh included 974,693 mesh elements.

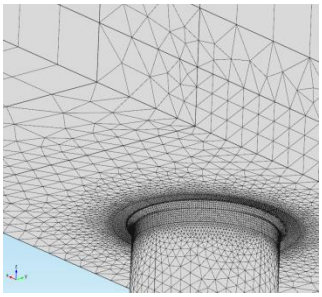

Figure 16: Mesh 2.

Mesh 3

Mesh 1 and 2 were compared to Mesh 3, shown in Figure 17, which exhibits only a free tetrahedral mesh and minimum interior boundaries. The interior cylinder boundary was the only feature inherited from Meshes 1 and 2. This decision was made because it was found that minimum mesh quality tends to bunch up on interior boundaries. The nozzle geometry was built as a plug into the combustor, so that there would be no boundaries attached to the fillet radius, and therefore the mesh would grow freely from the radius.

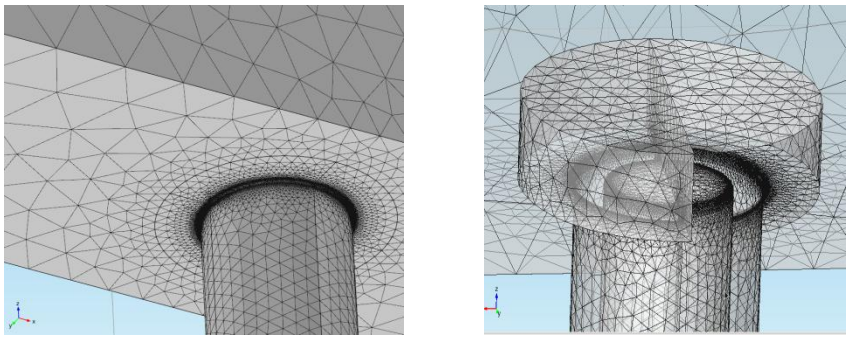

Figure 17: Mesh 3.

With a radius of *R=0.02D*, Mesh 3 exhibited the most efficient and accurate mesh, with only 374,705 elements and a mesh quality greater than 0.55 on the *x*-*z* plane.

The three meshes were compared by calculating the pressure difference between the three meshes along a line on the wall of the nozzle, leading up to the combustor, as shown in Figure 18 below.

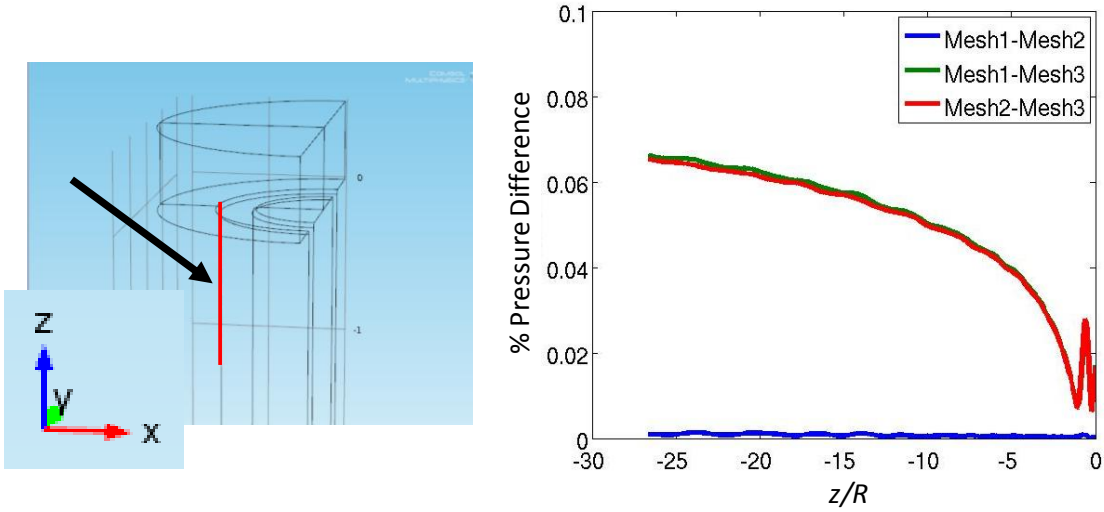

Figure 18: Location (left) and results (right) of mesh dependancy study.

From this study, it was found that the difference in pressure between the various meshes were well under the threshold of 1% difference. In fact, these results remained under 0.1% difference.

Most importantly, it is desired to use the smallest radius possible, while still including enough elements on the face of the radii. Mesh 3 was so space efficient, that it was able to calculate results using an inlet fillet radius of *R=0.01D*. Since Mesh 3 includes no mapping, we must choose the mesh based on observation of the mesh elements along the fillet radius.

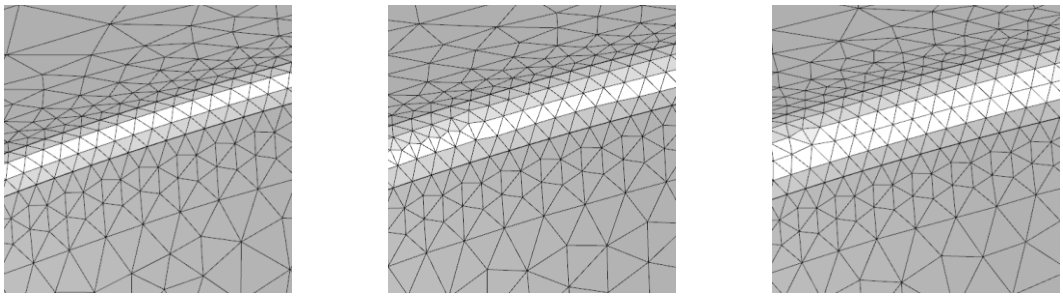

Figure 19: Assessing adequate mesh on fillet radius for *R/D*=0.01 (left), *R/D*=0.015 (center) and *R/D*=0.02 (right).

All of the above radii exhibit a minimum cross-sectional mesh quality of about 0.5565. So it was decided to use *R=0.02D* for the final inlet radius.

A model tolerance study was also completed by varying the relative tolerance from 1×10^{-3} to 1×10^{-7} for Mesh 1 with an *R=0.02D* radius. Results remained the same for all tolerance values, and showed no dependency on tolerance.

Symmetry Study

While analyzing the results of Mesh 3, discussed in the following sections, the symmetry of the mesh was brought into question. This is a reasonable doubt, as a free tetrahedral mesh could be less symmetric than the mapped mesh of Meshes 1 and 2. Therefore, Mesh 4 was designed to improve the symmetry of the model.

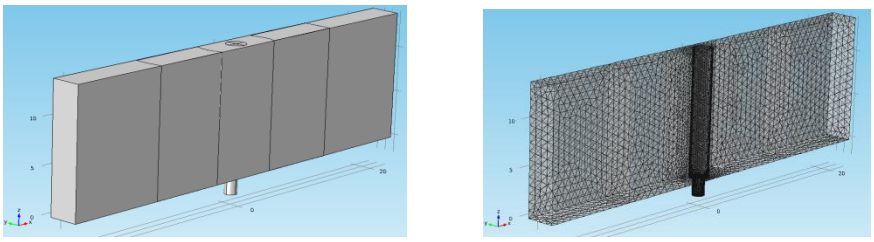

Figure 20: Mesh 4.

Mesh 4, shown in Figure 20 above, includes cylindrical interior boundaries designed to retain symmetry. As a consequence, the number of mesh elements increased to 1,058,926 elements, and the minimum element quality decreased slightly near the interior boundaries. Since a rightward travelling wave should be an exact mirror image of a leftward travelling wave through this combustor, a symmetry study was performed by calculating the difference between the rightward travelling wave and the mirror image of the oppositely travelling wave for both Mesh 3 and Mesh 4. Results of this study are shown in Figure 21 below.

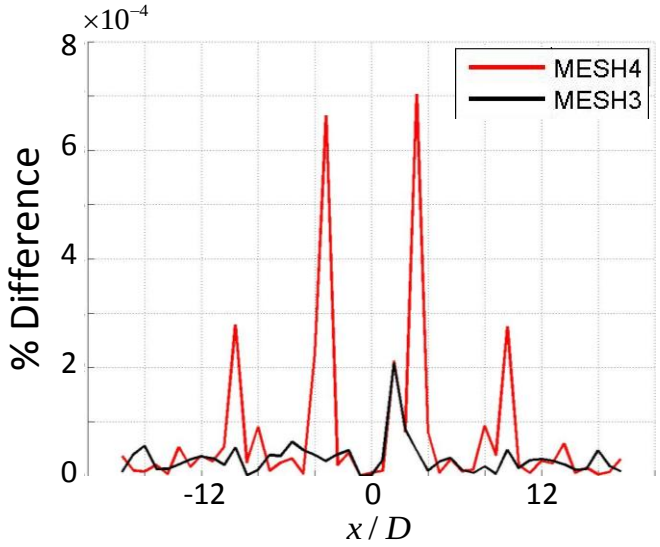

Figure 21: Calculated difference between travelling waves at *z*=0" above the nozzle inlet.

The results of the symmetry study were quite surprising. The difference between plane waves actually peaked at the interior boundaries, further indicating that interior boundaries introduce error in acoustic simulations and should be avoided. However, all

difference values remained below 8×10^{-4} %. Since velocity magnitudes are typically on the order of 10^{-3}, both meshes were deemed acceptable. Mesh 3 is still preferred due to its already tested efficiency and accuracy.

As discussed, the *R=0.02D* radius used for this study was chosen based upon the need to maintain a suitable mesh, while also minimizing the fillet radius. The resulting mesh is comprised of 374,705 free tetrahedral mesh elements and 529,592 degrees of freedom, and employs minimum interior boundaries. It was found that this configuration allows the mesh elements to grow freely from the small radius to the large combustor box with maximum efficiency and accuracy. The finite element mesh used for this study is shown in Figure 22 below.

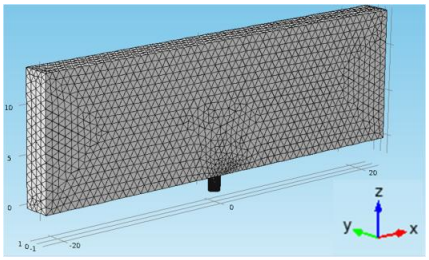

Figure 22: Finite element mesh.

CHAPTER 3

RESULTS AND VERIFICATION

This chapter presents typical results. Results were obtained for a range of frequencies between 200-3000 Hz, corresponding to non-dimensional D/λ values ranging from 0.02 to 0.3. These frequencies were simulated for the three forcing configurations and using the three upstream nozzle impedance values described in the previous section.

Near Field Results

Figure 23 illustrates the coordinate system and various cuts used to represent the three-dimensional disturbance field very near the nozzle-combustor junction.

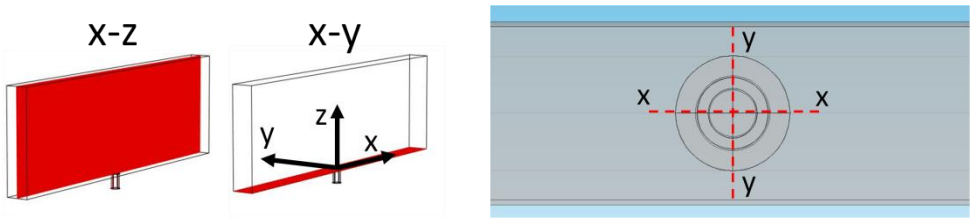

Figure 23: Schematics showing coordination system used to define different cuts at which data is plotted.

Figure 24 presents representative instantaneous pressure contours and velocity vector fields for the various forcing configurations, using an anechoic nozzle impedance. Results are shown on the *x*-*z* cut plane. The in-phase case, shown on the left, generates zero transverse velocity at the nozzle outlet, but large pressure fluctuations are present that are symmetric across the centerline. These pressure fluctuations lead to symmetric, axial velocity disturbances on both sides of the annulus. As we will discuss later, the nozzle response for this in-phase forcing case can be understood from quasi one-dimensional concepts. In contrast, the out-of-phase case exhibits large transverse velocity

fluctuations in the center of the combustor. Because of the centerline pressure node, the pressure fluctuations have a 180 degree phase difference on the two sides of the annulus. Similarly, the axial velocity fluctuations are phased 180 degrees apart on the left and right sides of the annulus. This nozzle response cannot be understood from quasi one-dimensional considerations.

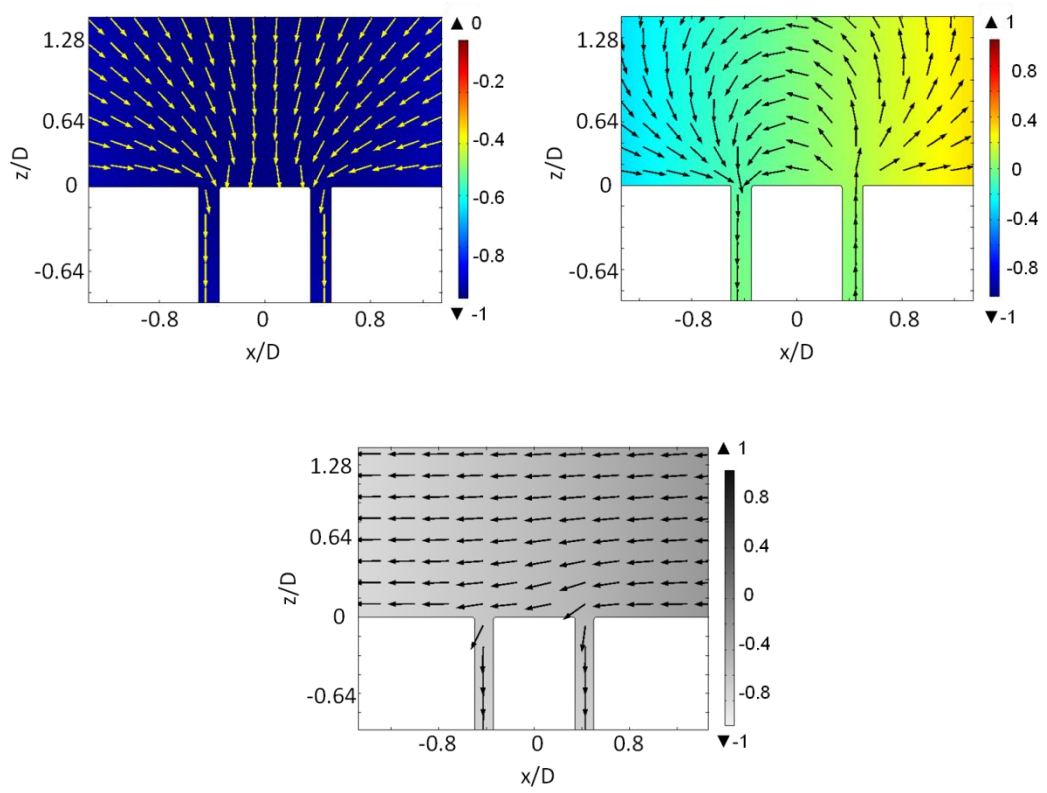

Figure 24: Instantaneous disturbance fields at 400 Hz with an anechoic boundary condition at the nozzle for in-phase (upper left), out-of-phase (upper right), and traveling wave (center) scenarios. Colors represent instantaneous pressure, while arrows denote the instantaneous total velocity field.

The traveling wave case shows an intermediate behavior. Because the wavelength is long relative to the nozzle, the disturbance field is nearly uniform across the nozzle. However, a slight phase difference in axial velocity fluctuations exist on the two sides of the annulus, evident in Figure 24. In addition, there is a slight amount of asymmetry in wave magnitudes on the two sides of the nozzle due to wave reflection. This traveling

wave scenario simulates the classical problem of wave reflection of an incident wave by a side branch [35]. In short, an acoustic wave incident on this boundary will generate both a reflected and transmitted wave. This is a similar approach taken for material boundaries.

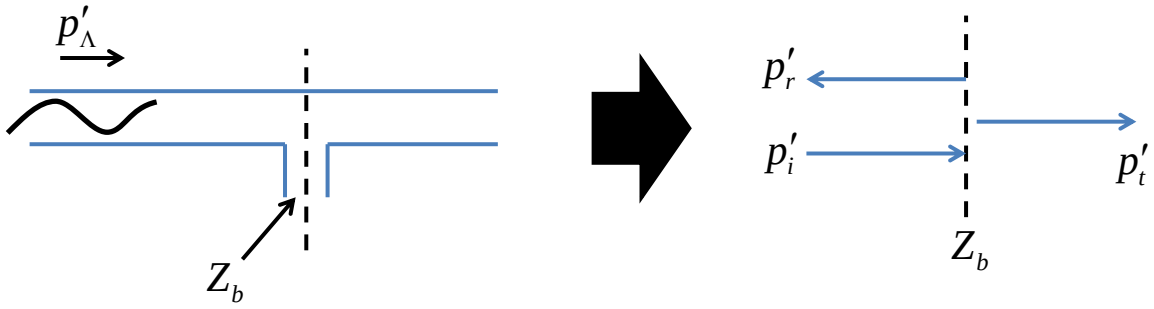

Figure 25: Modeling a side branch as an impedance boundary.

If we assume that the branch is short and unflanged, also representing a high pass filter, the equation for the impedance boundary generated by the branch is given by [35]:

$$Z_b = \frac{\rho c k^2}{4\pi} + i\frac{\omega \rho L_0}{\pi a^2} \tag{11}$$

where ρ and c are material properties, k is the wavenumber, ω is the angular frequency, a is the radius of the nozzle, and L_0 is the effective length of the nozzle, given by:

$$L_0 = l + 1.4a \tag{12}$$

The equation for branch impedance is used to calculate the reflected and transmitted pressure, as [35]:

$$p'_r = \frac{-\rho c / 2S}{\rho c / 2S + Z_b} p'_i \tag{13}$$

$$p_t' = \frac{Z_b}{\rho c / 2S + Z_b} p_i' \tag{14}$$

where S is the cross-sectional area of the side branch, and the incident pressure for the plane wave is given by:

$$p_i' = p_0' e^{-ikx} \tag{15}$$

The incident, reflected, and transmitted waves can be plotted below:

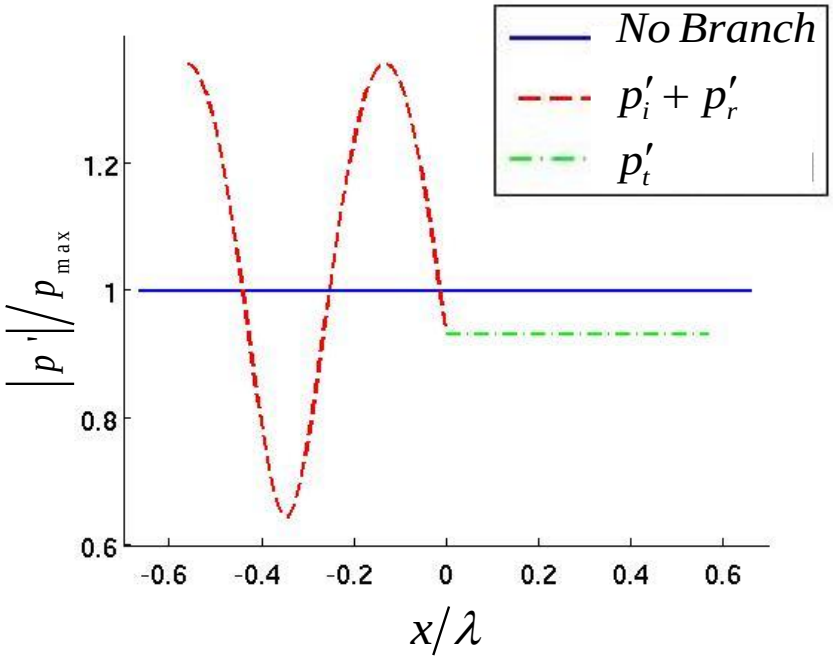

Figure 26: Theoretical pressure for a 400Hz incident traveling wave passing over a side branch with an anechoic exit.

By plotting this in MATLAB, the wavy, then flat nature of the traveling wave pressure is evident over the nozzle. This can also be observed by plotting these components together in COMSOL.

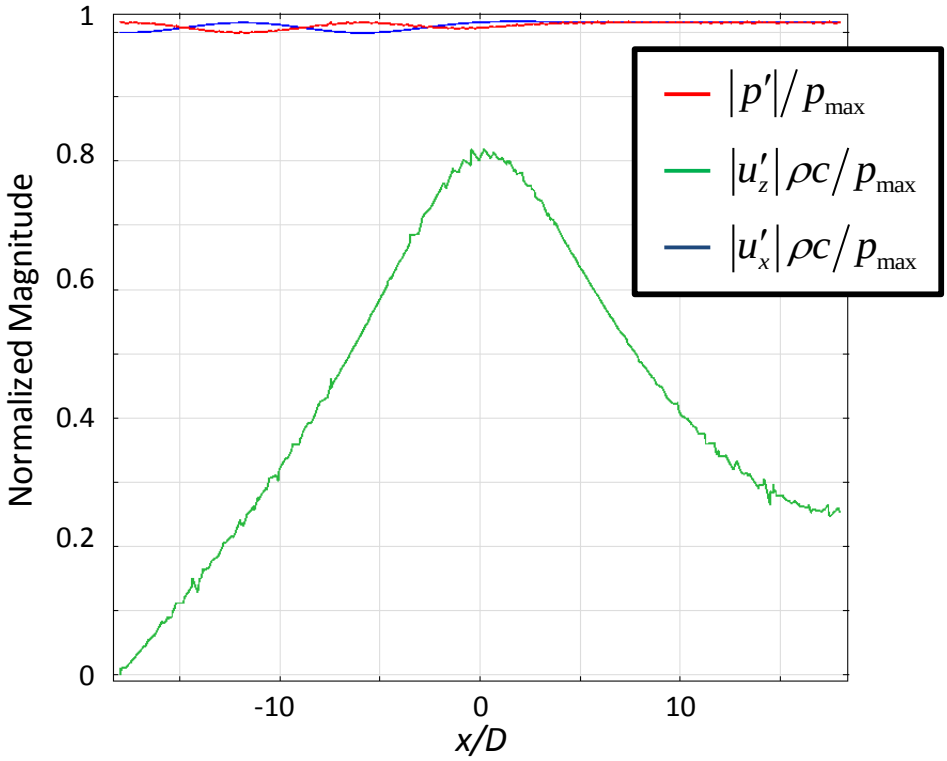

Figure 27: Simulated pressure, and transverse and axial velocity passing over a side branch at 400Hz with an anechoic exit.

Therefore, as the travelling wave passes over the nozzle, energy is shifted from the transverse pressure and velocity to the axial velocity component. In other words, axial velocity is generated at the nozzle and then propagates downstream.

It is important to note that the branch approximation is only applicable when the cross-sectional area of the branch is of similar magnitude of the cross-sectional area of the main channel. For our combustor model, this is not the case. However, we can use a simple 2-D COMSOL simulation to observe how the complex pressure field responds as the 1-D branch approximation becomes less valid, as shown in Figure 28.

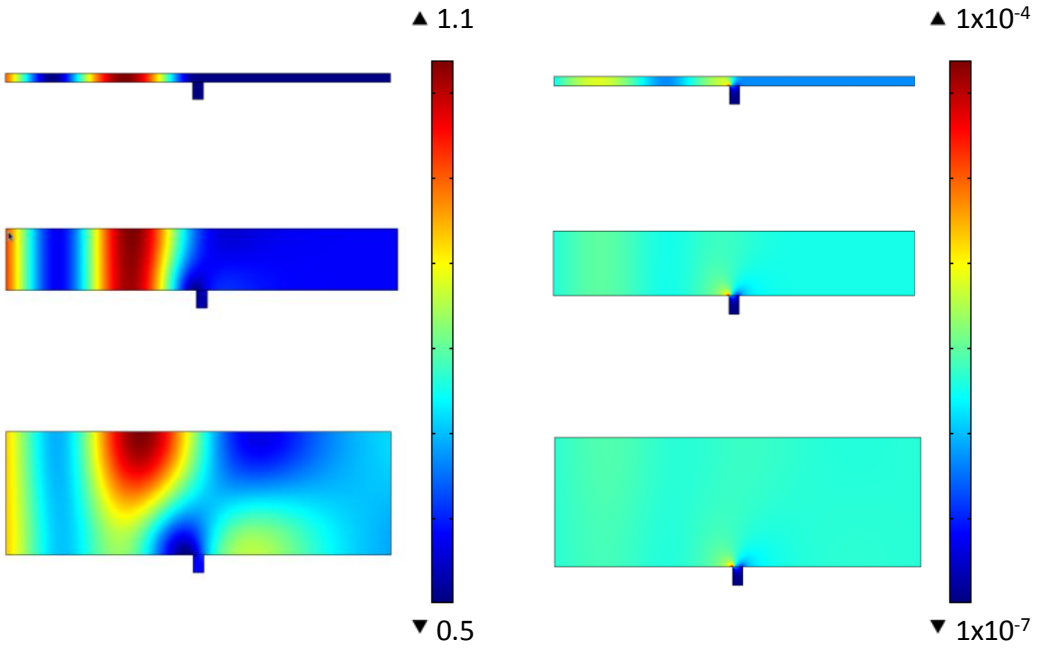

Figure 28: Evolution of pressure (left) and transverse velocity (right) at 400 Hz for a traveling wave with anechoic boundary condition. Color describes pressure and velocity, respectively.

From Figure 28, we learn that while the branch approximation allows us to make educated guesses about the acoustic field inside the combustor, a full 3-D acoustic simulation is necessary to capture all of the important physics.

This analysis also explains why a traveling wave scenario such as this is not necessarily physical inside an annular combustor with a spinning mode. With multiple nozzles, there will always be reflected waves trapped between two nozzles, so the traveling wave will actually lead to a field with a slight standing wave structure at each nozzle, as shown in Figure 29.

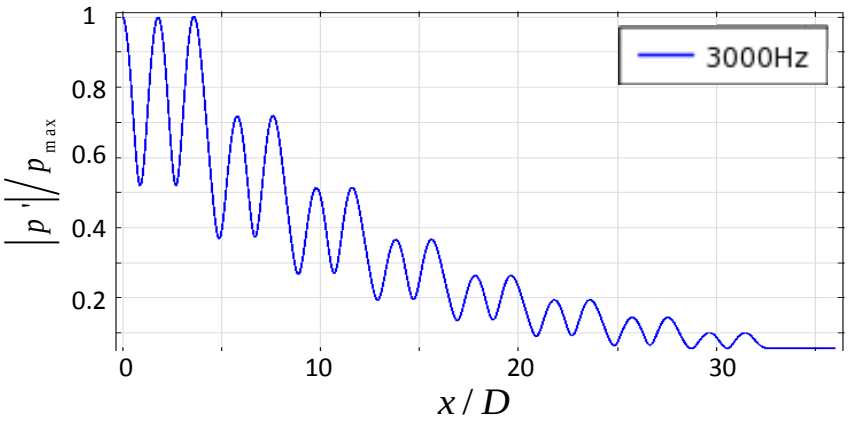

Figure 29: Traveling wave over eight nozzles at 3000Hz.

The azimuthal distributions of axial velocity magnitude and phase at the nozzle interface are shown in Figure 31, along with the accompanying pressure distributions along the bottom surface of the combustor shown in Figure 30. From this view, we can clearly see how the pressure anti-node at the center of the combustor excites evenly distributed axial velocity in the nozzle region. The phase reversal in axial velocity for the out-of-phase scenario can also be inferred from the node in the center. The traveling wave velocity distribution is asymmetric, exhibiting a much larger axial response on the right side of the nozzle.

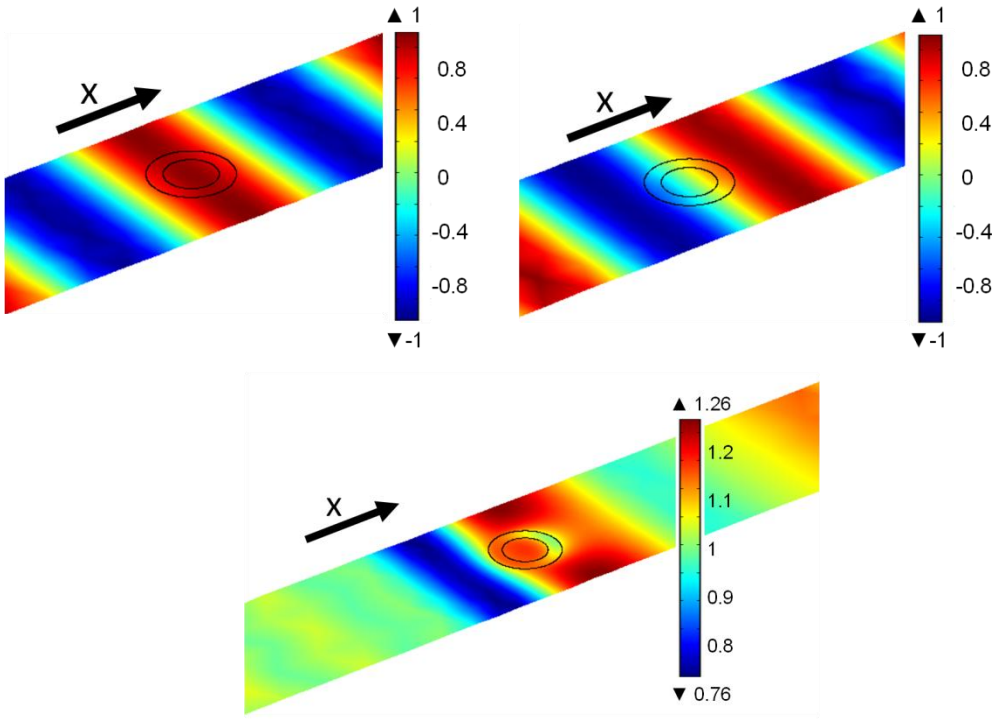

Figure 30: Three-dimensional instantaneous pressure along the *x-y* surface at 3000 Hz for in-phase (upper left), out-of-phase (upper right), and traveling wave (center) cases for anechoic nozzle impedance.

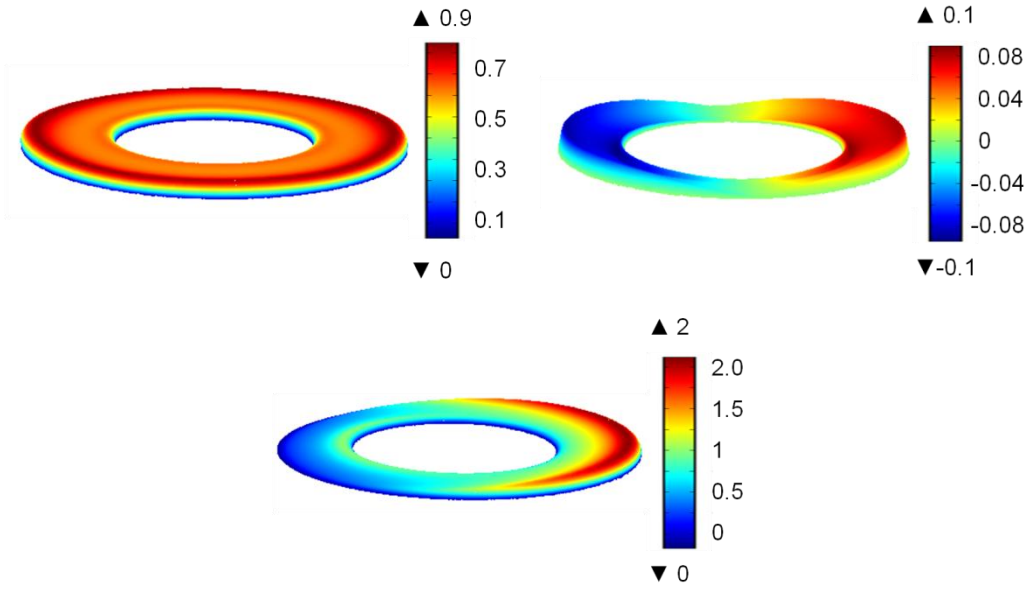

Figure 31: Spatial distribution of axial velocity magnitude at the nozzle-combustor junction at 3000 Hz for in-phase (upper left), out-of-phase (upper right), and traveling wave (center) scenarios for anechoic nozzle impedance. Color represents instantaneous axial velocity.

Pressure Field Analysis

As alluded to in the above discussion, important insights into the character of the axial velocity at the nozzle exit can be gained from the pressure field. As such, we next discuss the characteristics of the pressure field in the combustor section in more detail. Figure 32 presents plots of the magnitude of the pressure along the cut lines for a $Z_{tr}/\rho c = 1$ case. For reference, the solid line denotes the value of the disturbance field for a purely one-dimensional combustor acoustic field along the *x-x* cut line, representing the acoustic field that would exist in the absence of the nozzle. Note that for the anechoic condition, the nozzle causes only a slight distortion of the disturbance field.

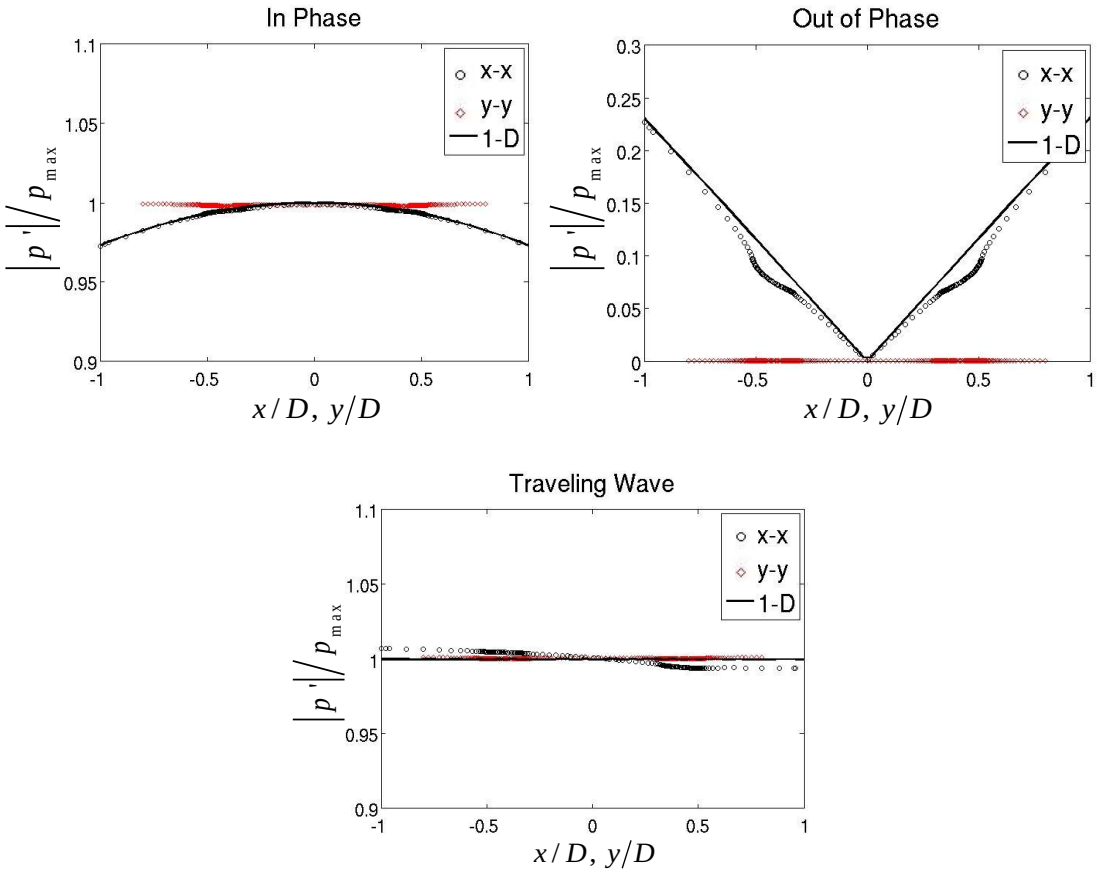

Figure 32: Pressure distributions at 400 Hz with an anechoic nozzle for the in-phase, out-of-phase, and rightward traveling wave scenarios.

Similar results occur for the $Z_{tr}/\rho c = 100$ case as shown in Figure 33 below, which approximates a rigid boundary condition at the nozzle.

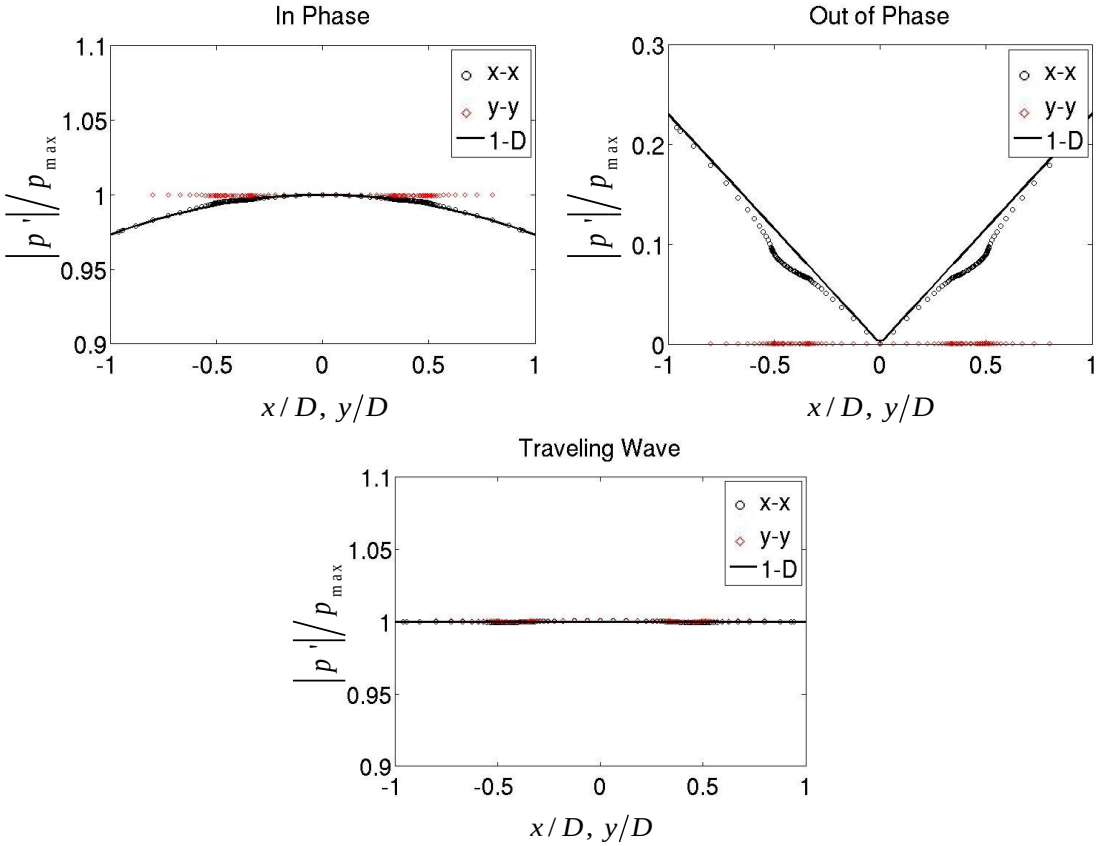

Figure 33: Pressure distributions at 400 Hz with a rigid nozzle for the in-phase, out-of-phase, and rightward traveling wave scenarios.

In contrast, the nozzle significantly distorts the pressure field from the 1-D result when $Z_{tr}/\rho c = 0.01$ for the in-phase and traveling wave cases, as shown in Figure 34. Little distortion occurs for the out-of-phase case where the nominal pressure field is zero. When the combustor acoustic field exhibits a significantly non-zero pressure near the nozzle note how the nozzle "pulls" the pressure amplitude toward zero.

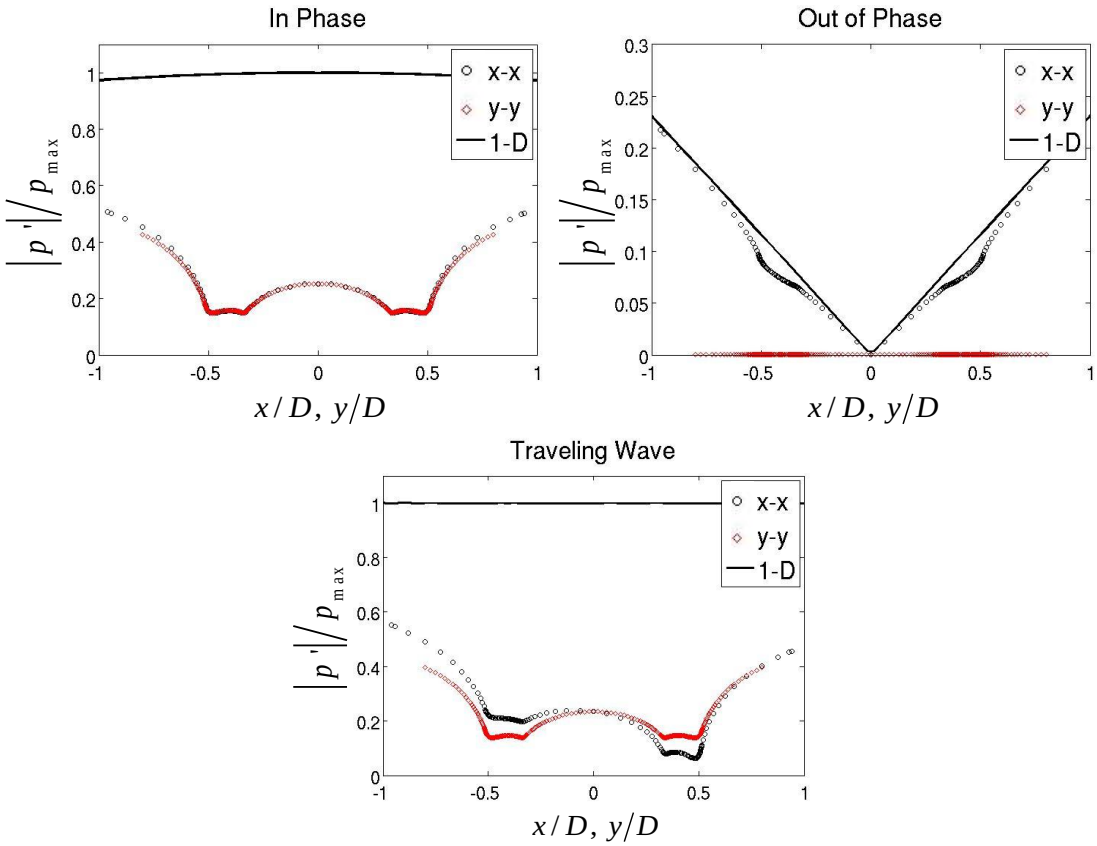

Figure 34: Pressure distribution at 400 Hz with a pressure release condition at the nozzle for the in-phase, out-of-phase, and rightward traveling wave scenarios.

Results for higher frequencies are shown in appendix A.

Velocity Field Analysis

Having discussed the pressure, we next consider the velocity field at the nozzle exit for the $Z_{tr}/\rho c = 1$ case. Figure 35 plots the in-phase result, along with the 1-D result on the *x*-*x* cut line. Similar to the nominal, one-dimensional result, the transverse velocity is low everywhere except near the annulus corners. Here, the sharp area change leads to a strong transverse velocity field. Note that the magnitudes of these velocity values near the corners are functions of the fillet radius, *R*. The axial velocity field is nearly uniform at the nozzle exit, reflecting a nearly plug flow disturbance field, except for overshoots near the corners, which are again functions of the fillet radius. No 1-D analogy for axial

velocity exists since these flow oscillations are purely multidimensional effects initiated by the nozzle geometry.

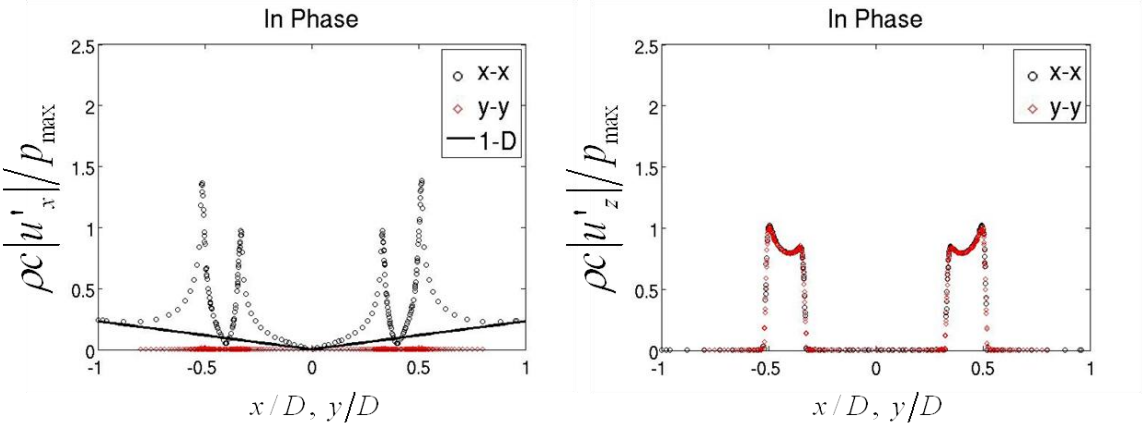

Figure 35: In-phase transverse (left) and axial (right) velocities at 400 Hz for an anechoic nozzle.

Similar results occur for the rigid approximation, where $Z_{tr}/\rho c = 100$. However, note the factor of ten decreases in y-axis values shown in Figure 36. The magnitudes of both velocity components are considerably decreased above the rigid nozzle, consistent with the change in boundary condition.

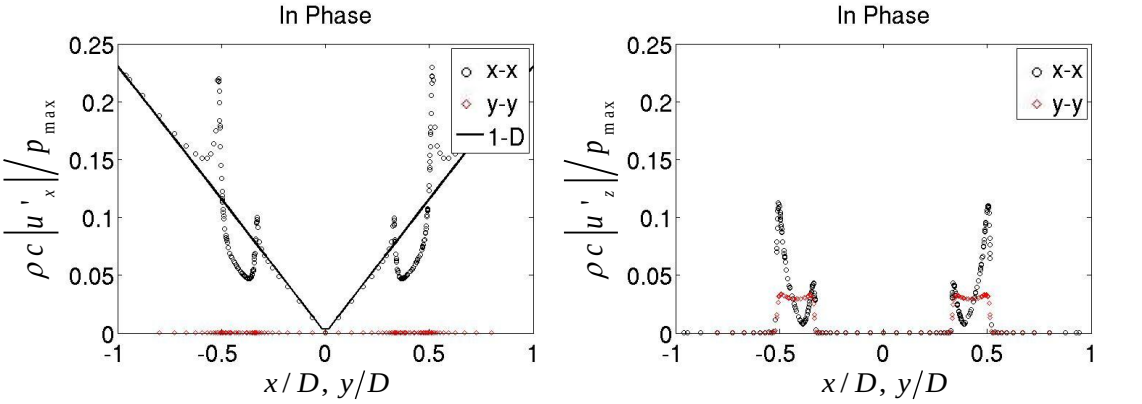

Figure 36: In-phase transverse (left) and axial (right) velocities at 400 Hz for a rigid nozzle.

Similarly, the velocity magnitudes are increased by a factor of ten for the pressure release nozzle, approximated by $Z_{tr}/\rho c = 0.01,$ as shown below in Figure 37. Again, results for higher frequencies are shown in appendix A.

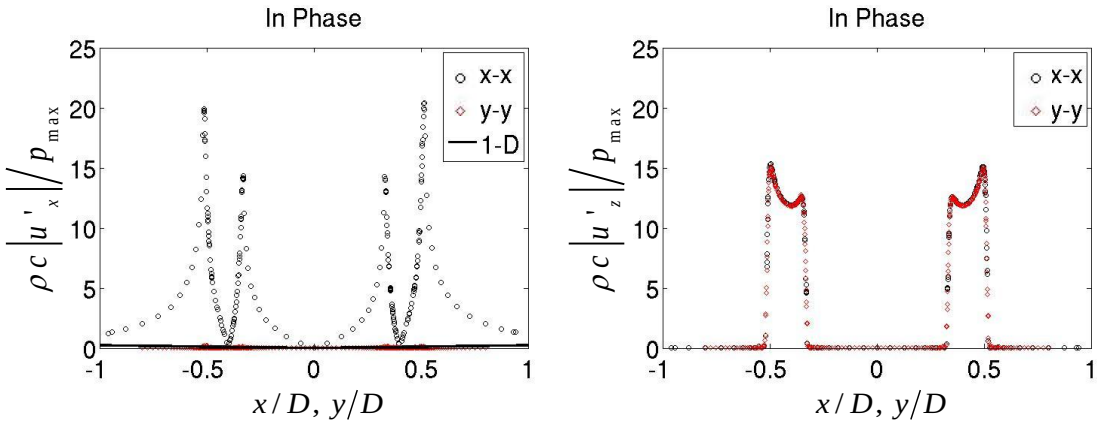

Figure 37: In-phase transverse (left) and axial (right) velocities at 400 Hz for a pressure release nozzle.

Transverse and axial velocity magnitudes for the out-of-phase and traveling wave forcing cases are shown in Figure 38 through Figure 43. Note that the largest axial velocities are observed near the outer edge of the annulus for the out-of-phase forcing case. As discussed previously, the values on the left and right sides are 180 degrees out-of-phase.

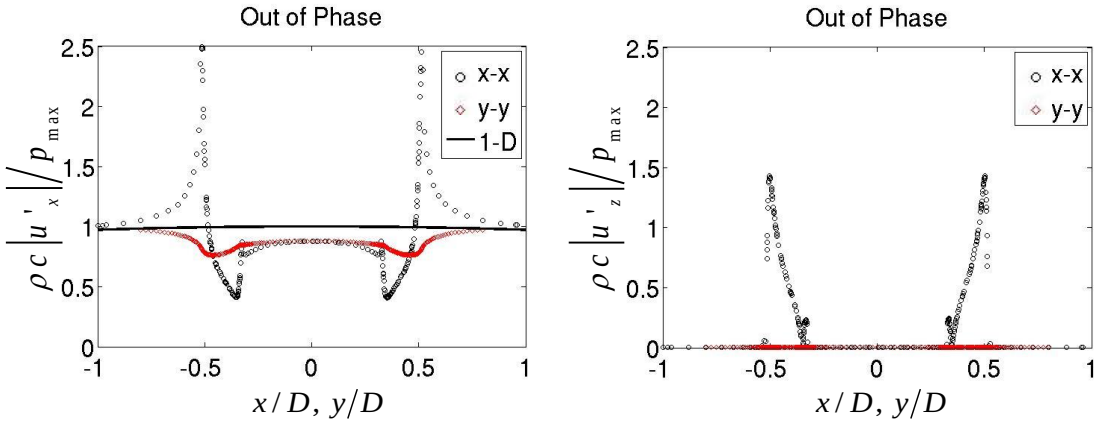

Figure 38: Out-of-phase transverse (left) and axial (right) velocities at 400 Hz for an anechoic nozzle.

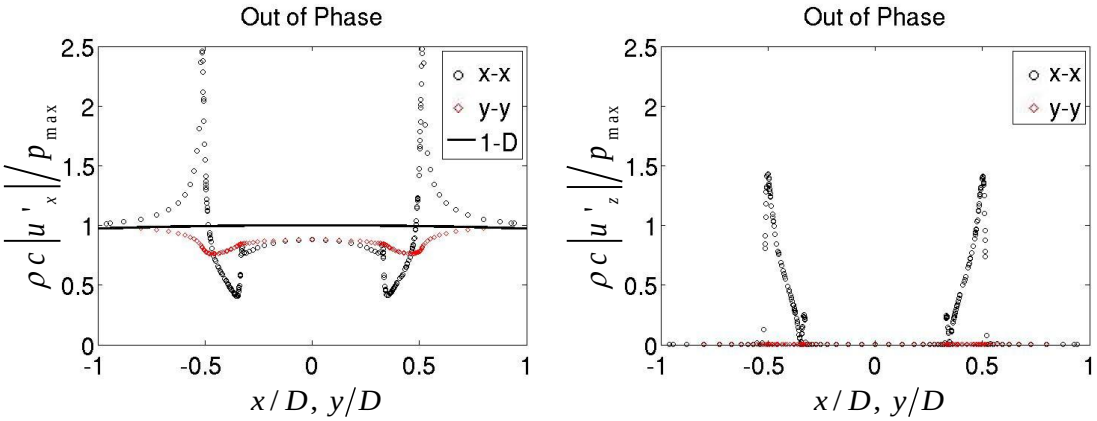

Figure 39: Out-of-phase transverse (left) and axial (right) velocities at 400 Hz for a rigid nozzle.

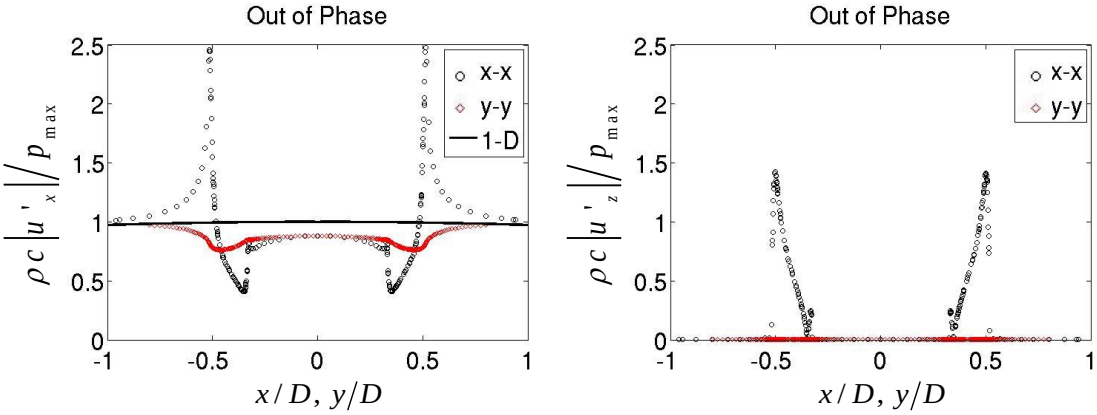

Figure 40: Out-of-phase transverse (left) and axial (right) velocities at 400 Hz for a pressure release nozzle.

Note that, for the out-of-phase forcing case, the magnitude of the velocity components do not change significantly with the various boundary conditions. It will be shown later that the out-of-phase results are actually less sensitive to the nozzle impedance, due to the pressure node at the nozzle center.

The traveling wave case results are asymmetric on the *x*-axis, as discussed previously. Along the *y*-*y* cut, the traveling wave displays the same shape and similar magnitude as those two sides of the nozzle experience the same disturbance field.

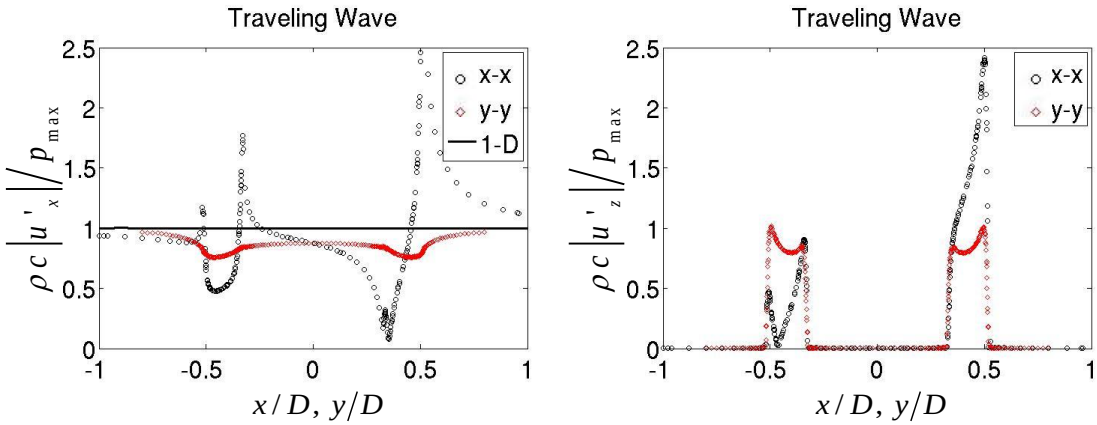

Figure 41: Traveling wave transverse (left) and axial (right) velocities at 400 Hz for an anechoic nozzle.

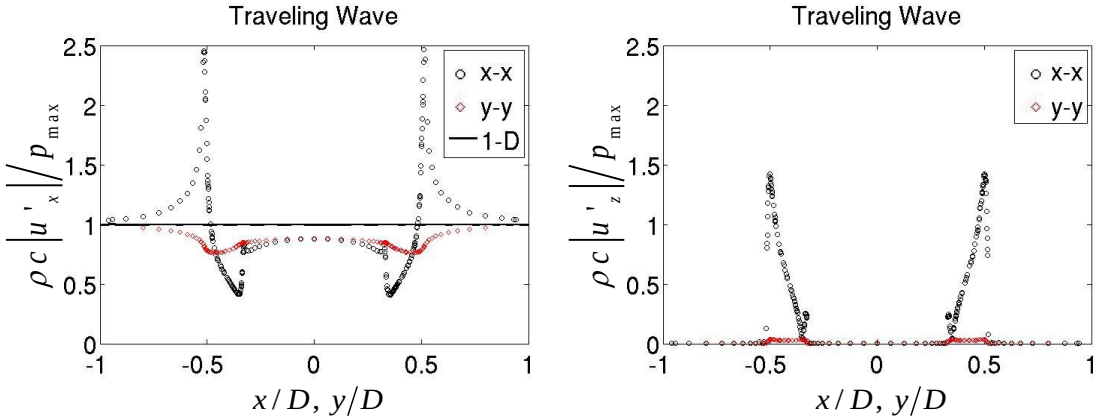

Figure 42: Traveling wave transverse (left) and axial (right) velocities at 400 Hz for a rigid nozzle.

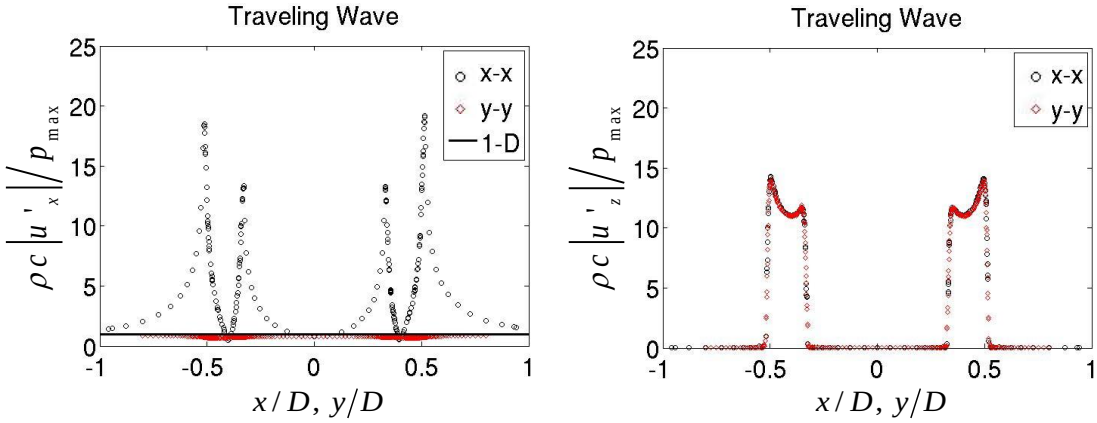

Figure 43: Traveling wave transverse (left) and axial (right) velocities at 400 Hz for a pressure release nozzle.

Interestingly, the traveling wave case can resemble either the in-phase forcing case or the out-of-phase forcing case or both, depending on the boundary conditions. For

the anechoic nozzle, the asymmetry of the traveling wave contains patterns from both the in-phase and out-of-phase standing waves on either side of the nozzle, as shown in Figure 41. However, with the rigid and pressure release boundaries at the nozzle, the traveling wave response becomes symmetric because the nozzle impedance dominates.

With the rigid nozzle, shown in Figure 42, the velocity patterns resemble that of the out-of-phase scenario. This makes sense because limited axial velocity is excited. In fact, even the in-phase case exhibits some of the out-of-phase velocity patterns when combined with a rigid nozzle. The traveling wave velocity component patterns above a pressure release nozzle are shown in Figure 43. These patterns look like those from the in-phase wave scenario, as axial velocity is excited consistently around the entire annulus. Results for higher frequencies for all cases are shown in Appendix A.

CHAPTER 4

FURTHUR ANALYSIS OF THE AXIAL VELOCITY

This chapter expands the analysis of the results of the axial velocity which, as discussed in the introduction, have been proposed as a particularly significant feature influencing how flames are excited during transverse instabilities. Here, we will further emphasize the role of nozzle impedance on these characteristics, and assess the extent to which quasi one-dimensional concepts can be used to understand the axial velocity characteristics at the nozzle exit.

Defining the Impedance Ratio

As discussed previously, the acoustic field in the nozzle quickly reverts to a one-dimensional field because the frequency is below the duct cut-off frequency. Once one-dimensional, the axial velocity and pressure in the nozzle are directly related by the translated nozzle impedance, Z_{tr}, given by equation (6). Thus, it is useful to define the impedance ratio, R_Z, through which to compare simulated results to quasi one-dimensional results, as:

$$R_Z = \frac{\overline{p'} \big/ \overline{u'_z}}{Z_{tr}} \tag{16}$$

The full Impedance Ratio equation, using theoretical impedance calculated using the one-dimensional impedance translation approximation in equation (6) is then given by:

$$R_Z = \frac{\dfrac{\overline{p}'}{\overline{u}_Z'}}{-\rho c\left[\dfrac{\left(-\dfrac{Z_o}{\rho c}-1\right)e^{-ik(z+h)}+\left(-\dfrac{Z_o}{\rho c}+1\right)e^{ik(z+h)}}{\left(\dfrac{Z_o}{\rho c}+1\right)e^{-ik(z+h)}+\left(-\dfrac{Z_o}{\rho c}+1\right)e^{ik(z+h)}}\right]} \tag{17}$$

Recall that the spatially averaged pressure and axial velocity were given by equations (9) and (8), respectively. While these expressions describe the pressure and velocity disturbance evaluated over one half of the nozzle, slightly different forms were used for different cases. It was shown in Figure 7 that the in-phase case leads to symmetric results on the two halves of the nozzle, and the out-of-phase case leads to anti-symmetric results. As such, integrating the pressure or velocity over the entire annulus area for the out-of-phase case leads to zero, because of cancellation of results on the two halves. Therefore, we use half the nozzle area, equations (8), (9), and (10), for the standing wave cases. The traveling wave case is integrated over the entire annulus face.

R_Z Validation

To validate R_Z, we utilize the fact that for a one-dimensional model, or a multidimensional model with no geometry change along an axial direction, p'/u' should always equal Z_{tr}, and so R_Z should always equal 1. R_Z was plotted using plane wave impedance, complex impedance, and frequency varying measured impedance boundary

conditions in order to prove that this is true for our derived impedance translation equation.

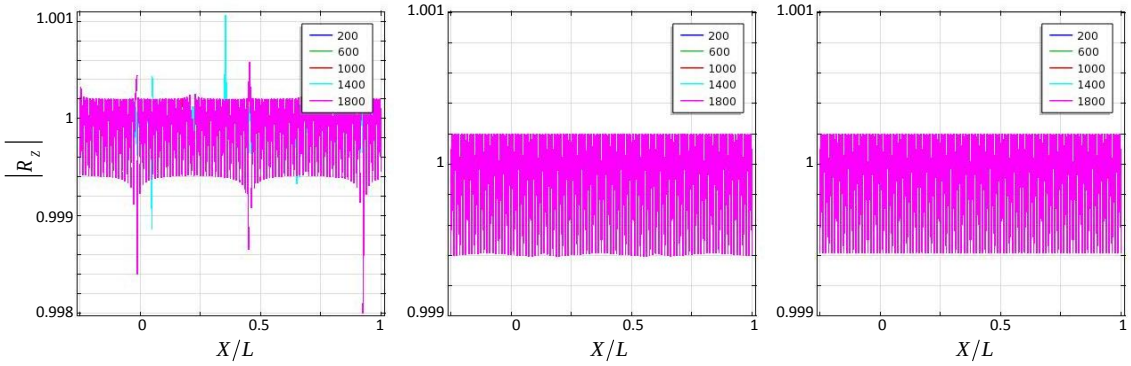

Figure 44: Impedance validation using measured impedance (left), complex $Z=(1+i)\rho c$ impedance (center), and plane wave $Z=\rho c$ impedance boundary conditions.

R_Z was also simulated for a 3-D model with no geometry change along the nozzle, to prove that this theoretical impedance and our use of the directional factor are correct for this model, as shown in Figure 45.

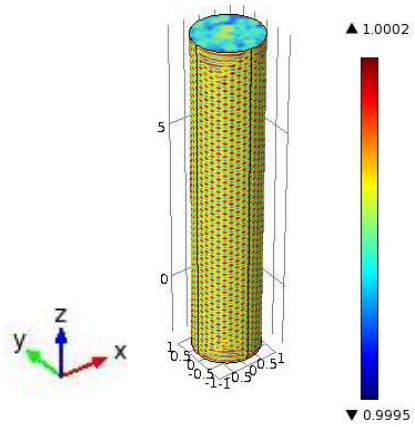

Figure 45: Three-dimensional impedance validation.

End Correction

Earlier it was stated that the added fillet radius has a large effect on the accuracy of the velocity calculation at the nozzle-combustor junction. The figures below show how

this small radius affects R_Z. For this study, we calculate average R_Z on a series of planes up the nozzle, shown in Figure 46.

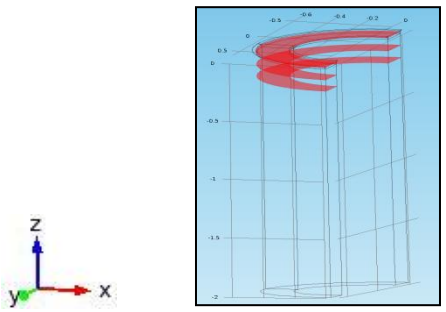

Figure 46: Data sets used to calculate averages along the nozzle in COMSOL.

Recall from Chapter 2 that axial velocity, u_z', was corrected by the changing area of the nozzle as the fillet radius was varied. This allowed the axial velocity to represent a constant flow rate through the nozzle. However, the pressure and transverse velocity were not corrected by the changing area because the pressure force above the nozzle remains constant. Therefore, the Impedance Ratio must also be scaled by an area ratio in order to achieve accurate results. Figure 47 through Figure 49 show the effect of this area ratio used to correct R_Z.

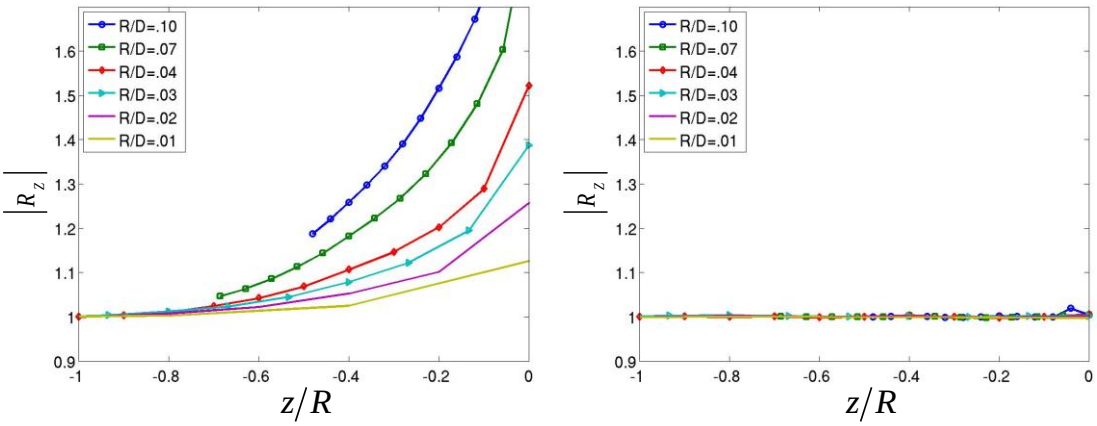

Figure 47: In-phase, anechoic R_Z results for 400Hz with (right) and without (left) the area ratio correction.

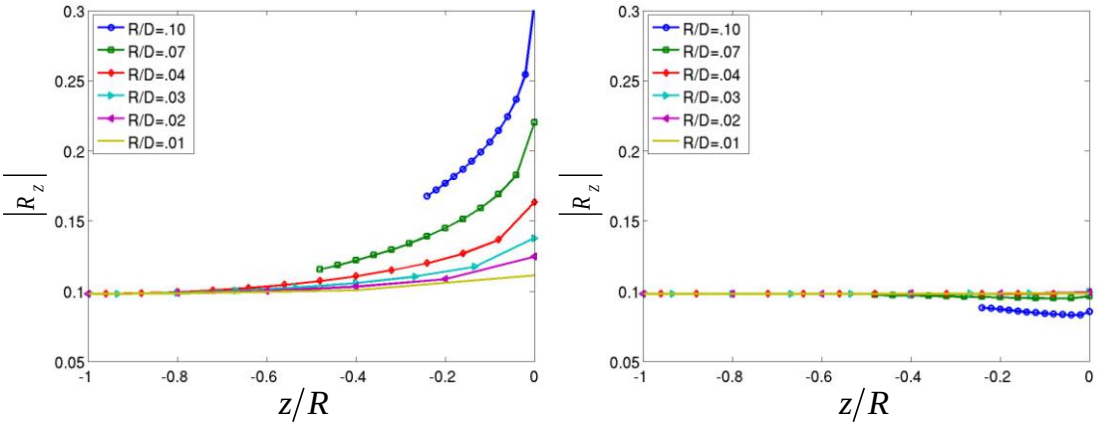

Figure 48: Out-of phase, anechoic R_Z results for 400Hz with (right) and without (left) the area ratio correction.

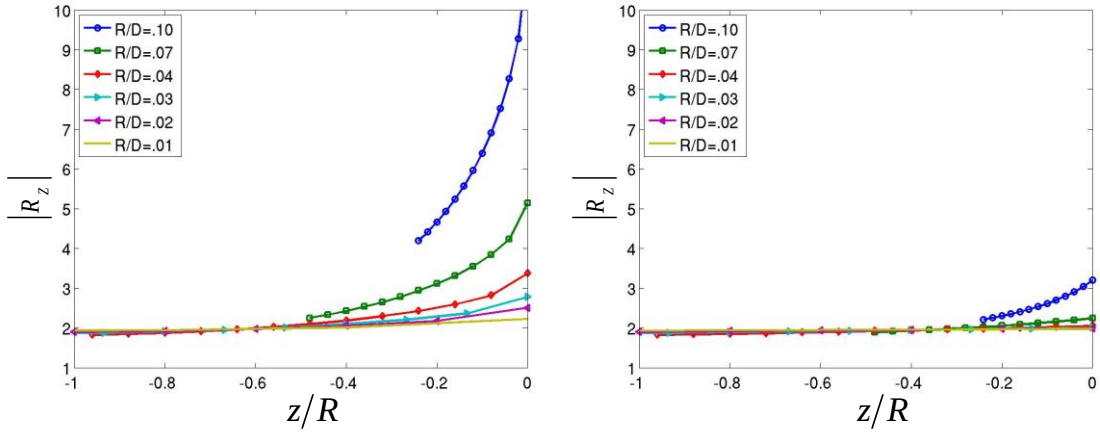

Figure 49: Traveling wave, anechoic R_Z results for 400Hz with (right) and without (left) the area ratio correction.

Furthermore, the same technique used in the radius study for the axial and transverse velocity components can be used to determine the radius dependency of R_Z, as shown in Figure 50 through Figure 52 below.

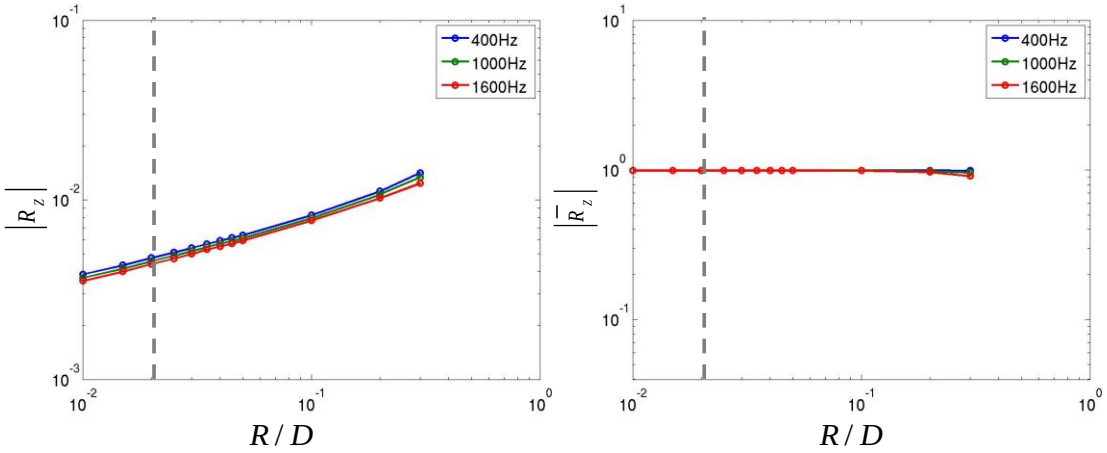

Figure 50: Dependence of impedance ratio at point D in Figure 6 (left) and spatially averaged over surface E in Figure 6 (right) upon fillet radius at three frequencies, for in-phase forcing with an anechoic nozzle.

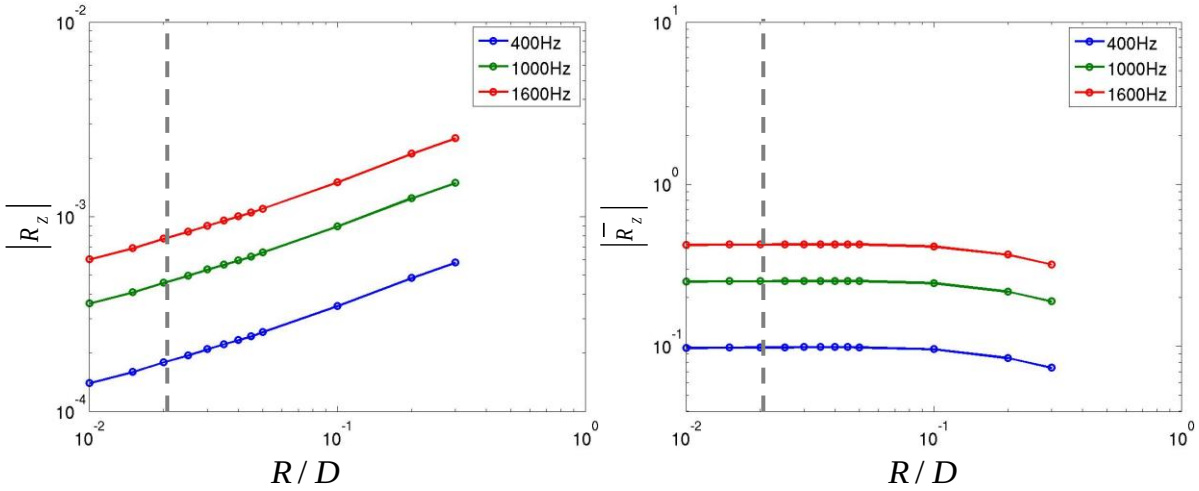

Figure 51: Dependence of impedance ratio at point D in Figure 6 (left) and spatially averaged over surface E in Figure 6 (right) upon fillet radius at three frequencies, for out-of-phase forcing with an anechoic nozzle.

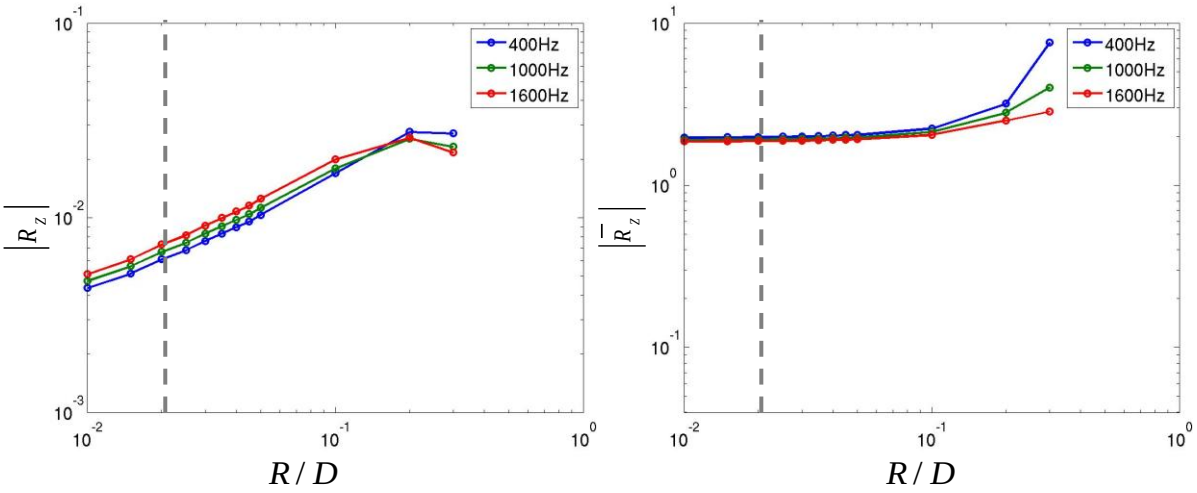

Figure 52: Dependence of impedance ratio at point D in Figure 6 (left) and spatially averaged over surface E in Figure 6 (right) upon fillet radius at three frequencies, for the traveling wave forcing scenario with an anechoic nozzle.

Standing Wave R_Z Results

R_Z data was calculated for the standing wave scenarios by taking average pressure and axial velocity on the half-annulus where the nozzle meets the combustor. As previously explained, the half-annulus is used because the in-phase wave is symmetric, and the out-of-phase wave is equal but opposite averaged on each side of the nozzle, and would therefore cancel on both sides. The half annulus used for data extraction is shown in Figure 53 below.

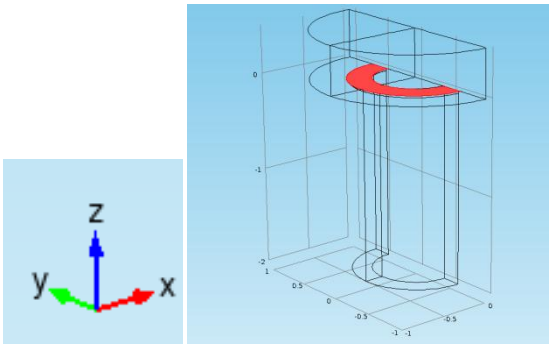

Figure 53: Domain used for averaging R_Z data in COMSOL.

Finally, we can observe how impedance ratio varies with frequency, as shown in Figure 54. Note that as the frequency increases and the wavelength shortens the pressure above the nozzle decreases, and so does R_Z.

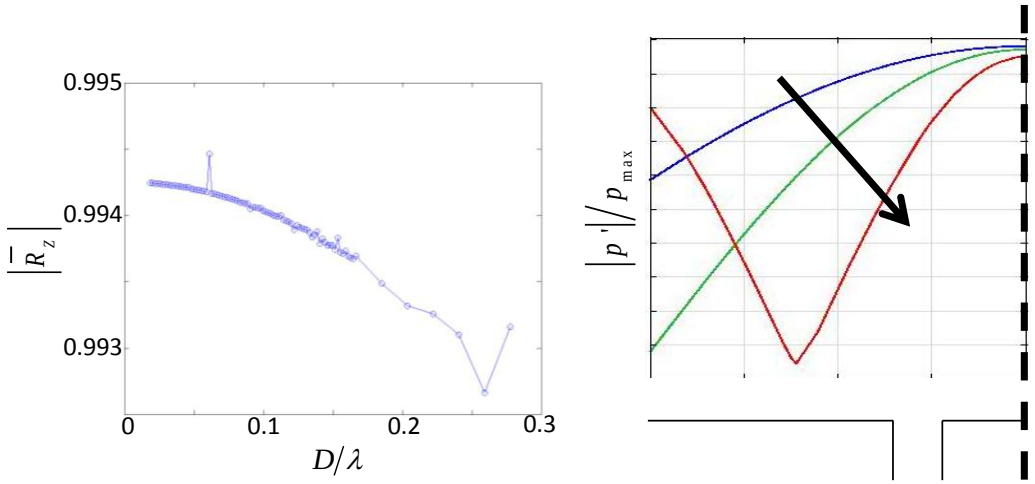

Figure 54: Impedance ratio for the anechoic, in-phase case vs. frequency.

For the out-of-phase case, the opposite trend occurs. As the pressure increases above the nozzle, R_Z is also increased, as depicted by Figure 55 below.

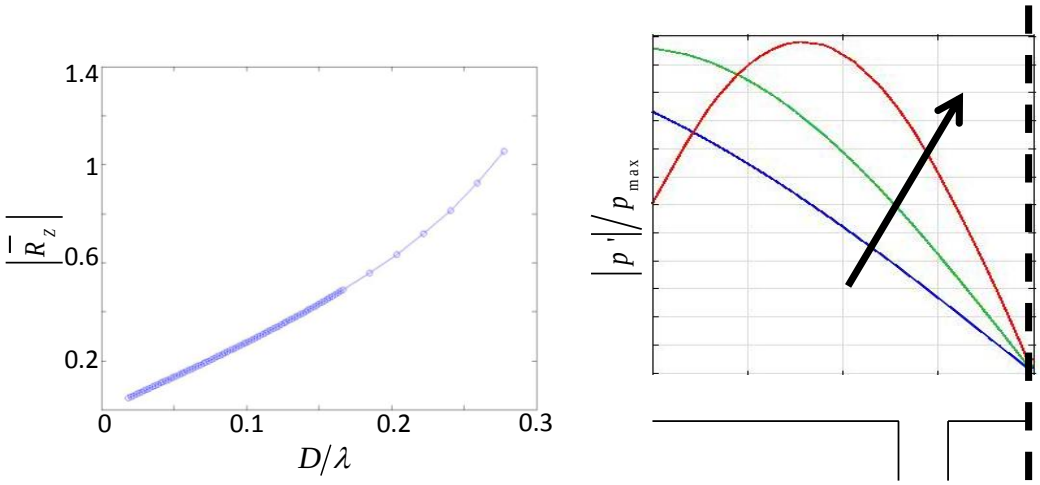

Figure 55: Impedance ratio for the anechoic, out-of-phase case vs. frequency.

Traveling Wave R_Z Results

As stated, R_Z for the traveling wave scenario was calculated on the entire annulus. Figure 56 below depicts this R_Z acting similar to the in phase result for the anechoic case.

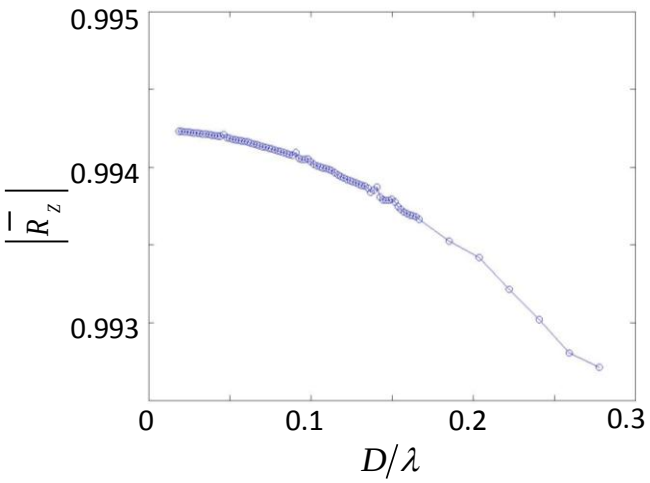

Figure 56: Impedance ratio for the anechoic, traveling wave case vs. frequency.

Additionally, the traveling wave R_Z is interesting in 2-D. Here, we see an asymmetric transition region, shown in Figure 57 below.

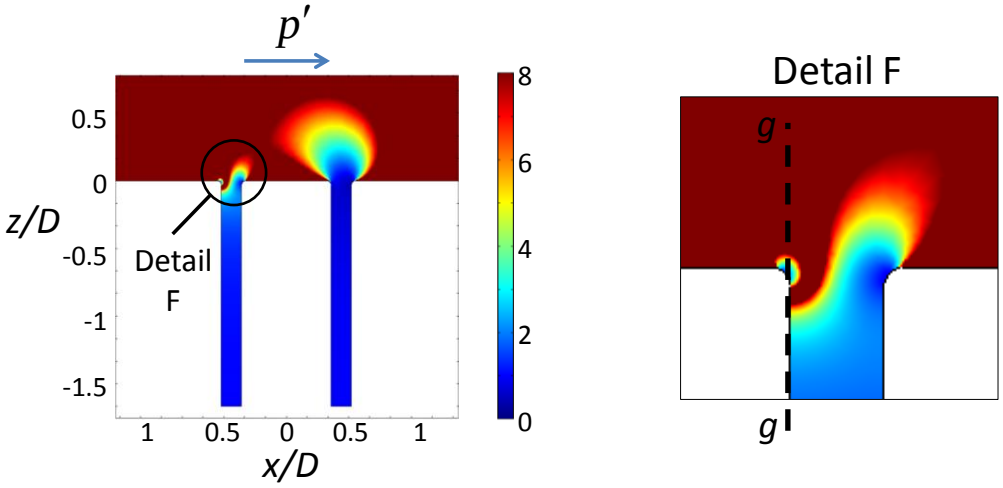

Figure 57: Impedance ratio transition region (left) for traveling wave at 400Hz with an anechoic nozzle. Detail F (right), includes the data set (line *g-g*) used for traveling wave R_Z results for this study.

Of all the cases observed thus far, results very near the fillet radius for the traveling wave case have shown the greatest dependency on fillet radius. Therefore, we wish to analyze the radius dependency of this specific feature. In order to do so, Meshes 1, 2 and 3 were compared by tabulating the maximum value of R_Z along line *g-g* through

the nozzle, very near the nozzle edge, during the travelling wave scenario. Results were also compared using both the forward traveling and reverse traveling waves from Meshes 2, 3, and 4, in order to validate the symmetry of the model. The vertical locations of the maximum R_Z values were also tabulated. This was done in order to observe the difference in mesh effects. As stated during the mesh development described in Chapter 2, it is important to ensure that the fillet radius geometry is adequately covered my mesh points as the radius is varied, to ensure mesh-independent solutions very near the fillet. Because Meshes 1 and 2 employ a mapped mesh on the fillet face, it was possible to hold six mesh points on the fillet as the radius was varied. For Meshes 3 and 4, care was taken to ensure that the fillet radius was covered by at least five mesh points for all radii sizes. The number of mesh points along the fillet, along with the wave direction, the maximum R_Z value along line *g-g*, and the axial location of this maximum R_Z value, are all tabulated in Appendix B for each mesh and radius size shown in Figure 58 below. It was observed that below a radius of about *R=0.02D*, all three meshes gave similar results.

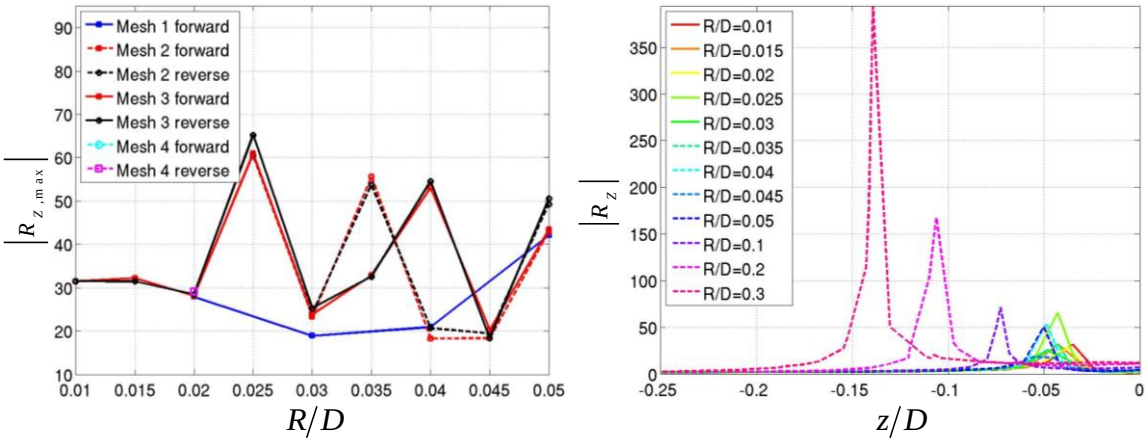

Figure 58: Plots showing the maximum R_Z values along line *g-g* vs. fillet radius for all meshes (left) and the location of this value as fillet radius varies for mesh 3 (right) for a traveling wave at 400 Hz with an anechoic nozzle.

The results of this study show that below a certain fillet radius value, the transition region becomes independent of fillet radius effects. This is an encouraging result, which states that even though the fillet radius can be a source of error very close to the nozzle-combustor junction for a traveling wave, there are many useful conclusions that can be drawn from this model that are radius independent.

R_Z vs. Frequency for All Cases

With the end correction in place, Figure 59 and Figure 60 plot the calculated dependence of R_Z upon the dimensionless frequency for both the traveling wave and in-phase forcing cases, respectively. Note how the magnitude of R_Z is quite close to unity. In both of these cases, the unsteady pressure field has nearly uniform phase across the entire face of the annulus, so it is expected that multi-dimensional effects in the nozzle are quite small. The growing, but slight, deviation of R_Z from unity with increasing frequency is a manifestation of the increasing phase or magnitude variation in unsteady pressure in the traveling and in-phase cases, respectively.

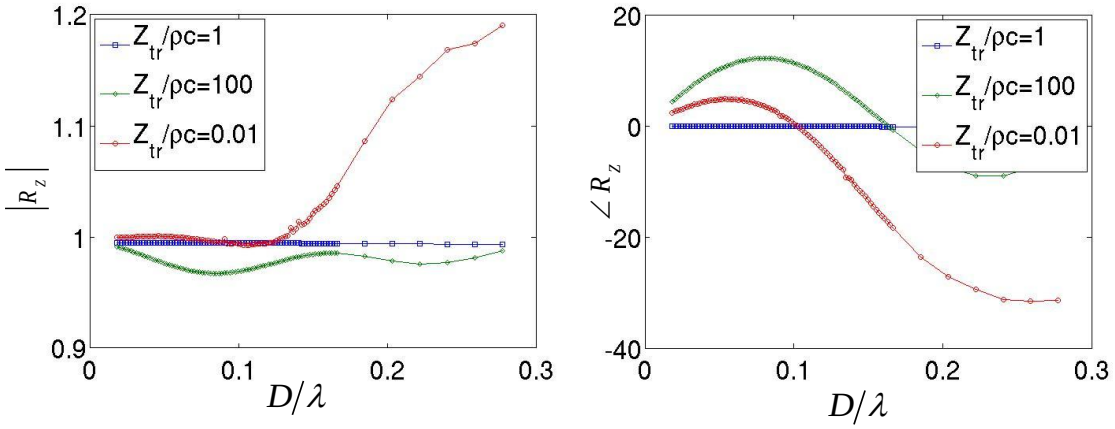

Figure 59: Impedance Ratio magnitude (left) and phase (right) for various nozzle boundary conditions at the nozzle for the traveling wave case.

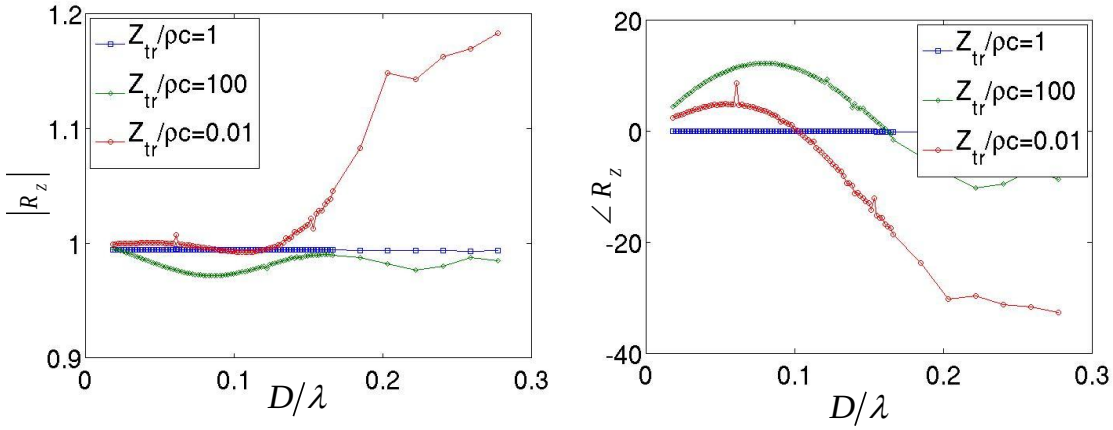

Figure 60: Impedance Ratio magnitude (left) and phase (right) for various nozzle boundary conditions at the nozzle for the in-phase forcing case.

Although not shown, R_Z deviates substantially from unity for the out-of-phase forcing case. Recall that for this case, there exists a 180 degree phase change in axial velocity and pressure on opposite sides of the vertical axis. If the two halves of the nozzle were physically separated by a rigid barrier, then R_Z would be a useful quantity and show values near unity. In actuality, the phase cancellation causes a vanishing of the acoustic field in the nozzle and, hence, renders the nozzle outlet velocity and pressure independent of the nozzle impedance. As such, R_Z is not a useful quantity for characterizing the axial velocity response. These points can be seen from Figure 61, which plots the ratio of the spatially averaged pressure and axial velocity over one half of the nozzle face as a function of frequency. Note that all three nozzle impedance values give the same pressure-velocity relationship at the nozzle exit.

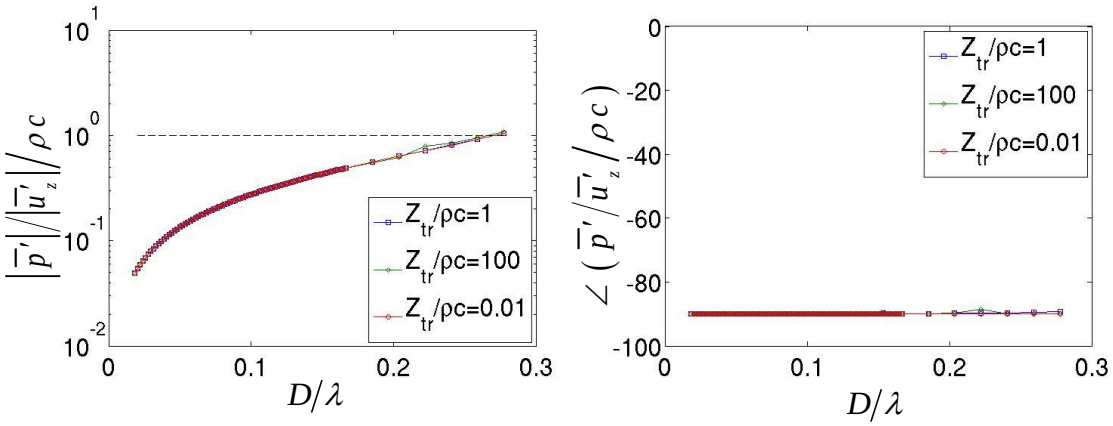

Figure 61: Spatially averaged nozzle impedance magnitude (left) and phase (right) for out-of-phase forcing for three nozzle impedance values.

CHAPTER 5

CONCLUSIONS AND RECCOMENDATIONS

Here we describe the conclusions from this thesis, and outline a number of recommendations for possible investigation in the future.

Concluding Remarks

This thesis has described an analysis of the coupling between transverse acoustic motions and the induced axial motions in a small area side channel, simulating the complex acoustic field generated by a fuel/air mixing nozzle inside an annular combustion chamber. The results put forth here display a critical dependence of the near-field acoustics on "macro" features of the acoustic field, such as the general waveform of the disturbance in the absence of the nozzle, or the location of the nozzle with respect to global velocity or pressure nodes. In addition, it was shown that nozzle impedance has a very significant effect on this transverse to axial coupling for in-phase and traveling wave acoustic excitation. The bulk features of the pressure field at the nozzle exit can be understood from 1-D acoustic considerations for several of the cases, due to the small cross sectional area of the side branch relative to that of the main chamber. An important exception to this occurs when the nozzle is nominally located in a pressure anti-node and the nozzle impedance attempts to force that same location into a pressure node, as was seen for an in-phase wave with a pressure release nozzle. Similarly, we show that the spatially averaged pressure to axial velocity relationship is quite close to the one-dimensional, translated impedance value at the end of the side branch. The notable

exception to this result occurs in the out-of-phase forcing case, whose axial velocity characteristics are independent of the nozzle impedance.

Recommendations for future work

The results presented in this thesis generate curiosity and motivation for further investigation. Therefore, recommendations for future work are presented here.

First, it would be of interest to observe much higher frequencies than those shown here. For example, frequencies whose acoustic wavelength is of the same order of the nozzle diameter may cause typical 1-D approximations to breakdown in the nozzle region, so more can be learned by simulating this condition. Of course, a very finely meshed model would be required to complete such a study.

Also, as discussed briefly, adding multiple nozzles to the combustor model can make for a more realistic traveling wave scenario. Therefore, it would be interesting to further analyze multiple nozzle effects for this case.

Additionally, there are a variety of ways to approximate the theoretical impedance at the nozzle-combustor junction, and these methods should be investigated. For example, the axial velocity excited in the nozzle could be visualized as a velocity driven baffled piston. Adapting the model to apply this condition could have significant benefits and shortcomings which should be considered.

Finally, recall that in order to remove the singularities generated by a sharp inside corner during the inviscid simulation, a fillet radius was added at the nozzle-combustor junction. While this modification helped to remove the singularity for this model, it should be noted that numerical alternatives exist to remove this singularity, and these alternatives may be more accurate very near these corners. Specifically, the unsteady

Kutta condition [36] should be investigated to address this singularity and completely remove the fillet radius feature. Such a modification could greatly simplify the meshing work undertaken in this work, could improve the accuracy of simulated results at the nozzle-combustor junction, and could also be applicable to a much wider range of acoustic studies.

APPENDIX A

HIGHER FREQUENCY PRESSURE AND VELOCITY PLOTS

In-phase, Anechoic, 1600Hz

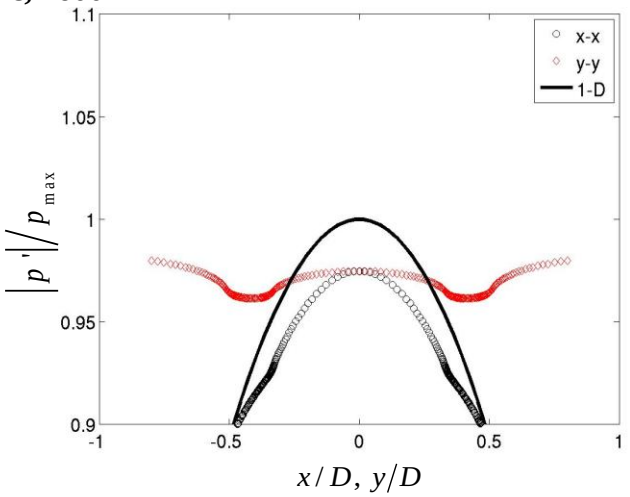

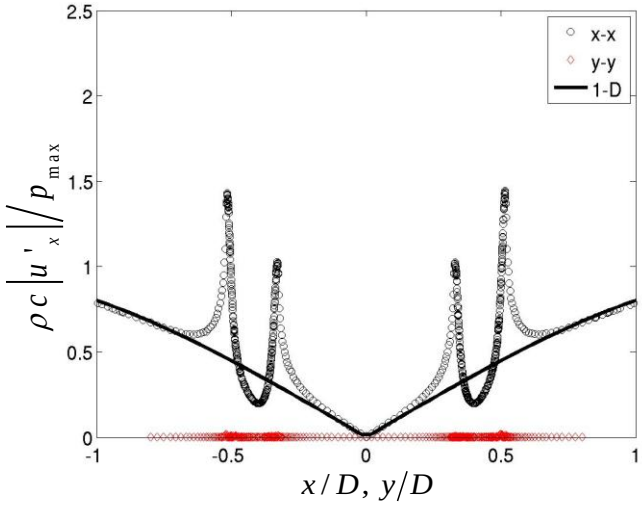

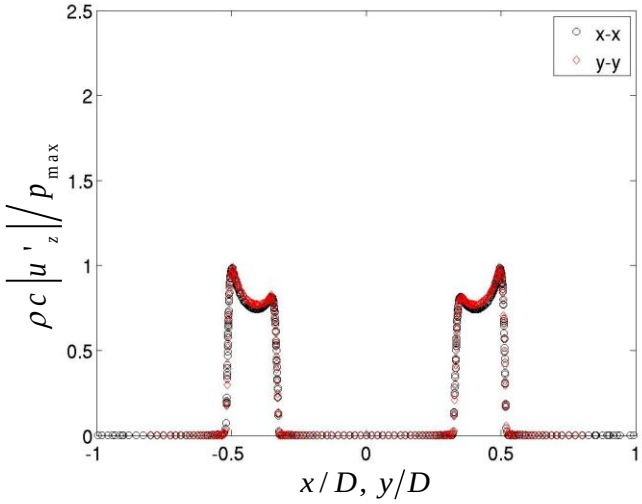

Out-of-phase, Anechoic, 1600Hz

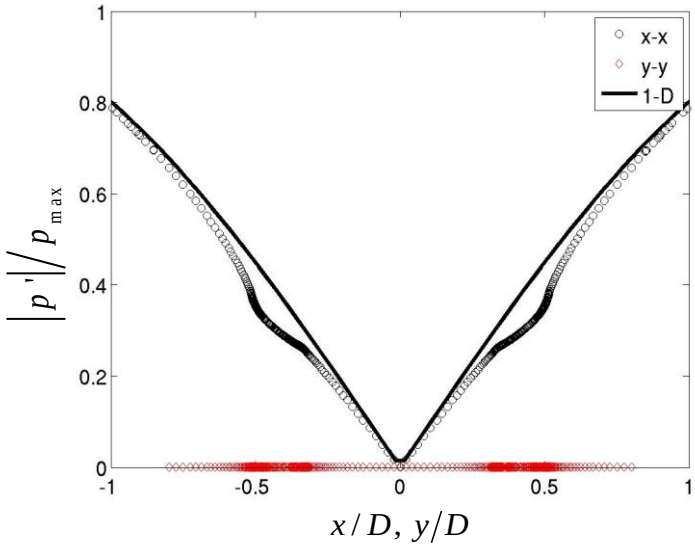

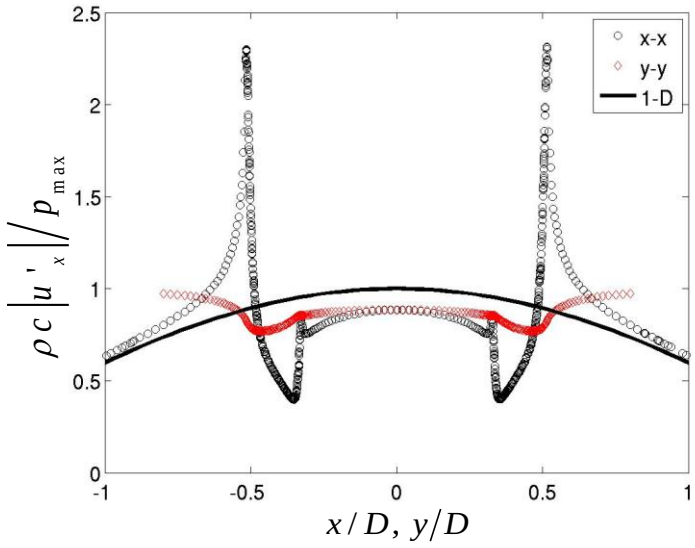

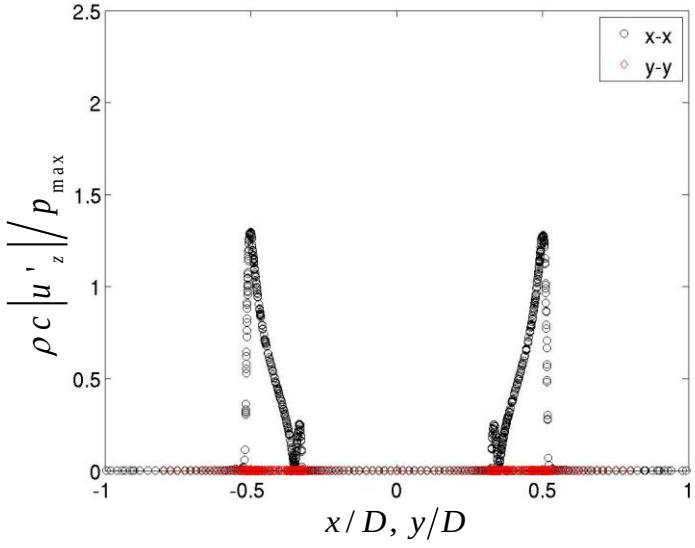

Traveling wave, Anechoic, 1600Hz

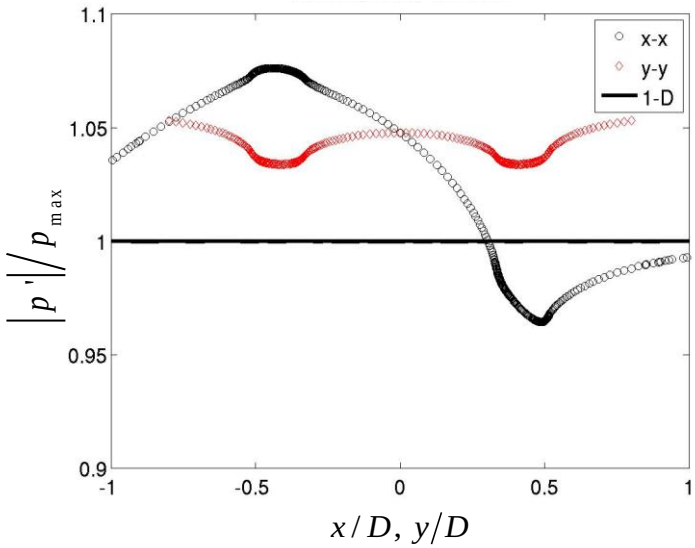

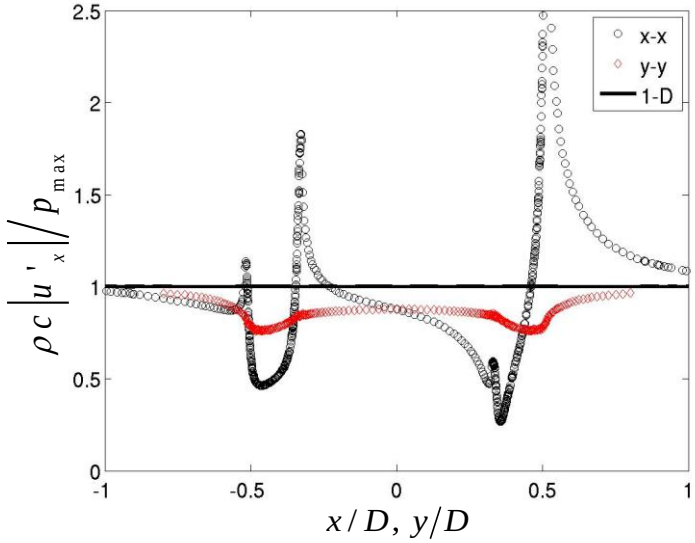

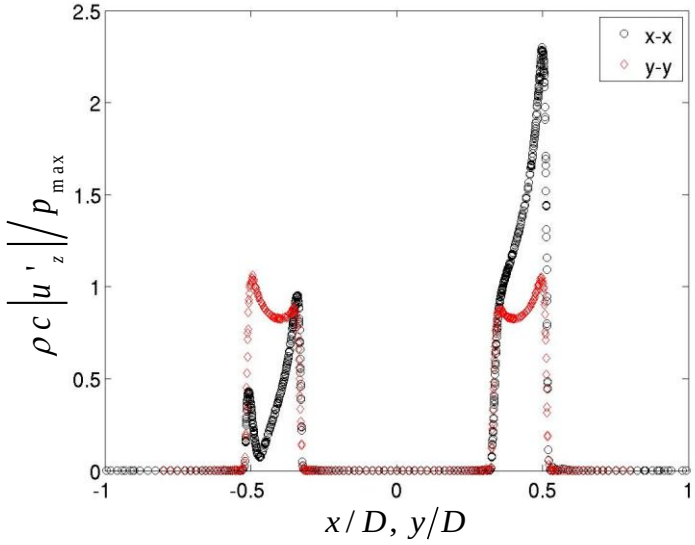

In-phase, Anechoic, 2800Hz

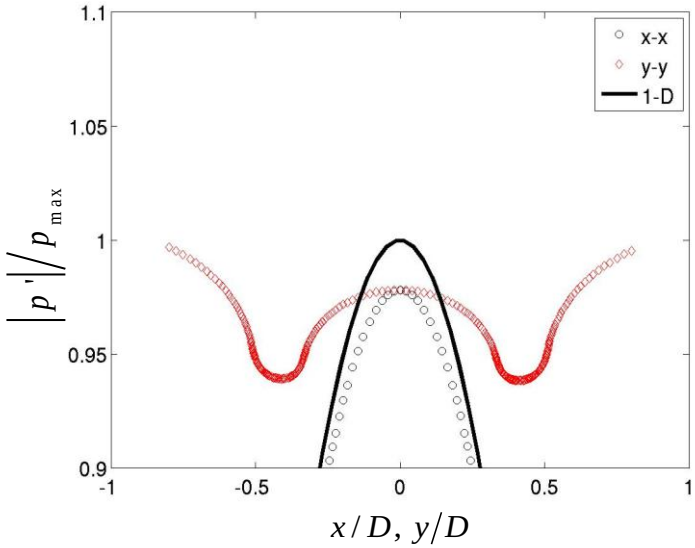

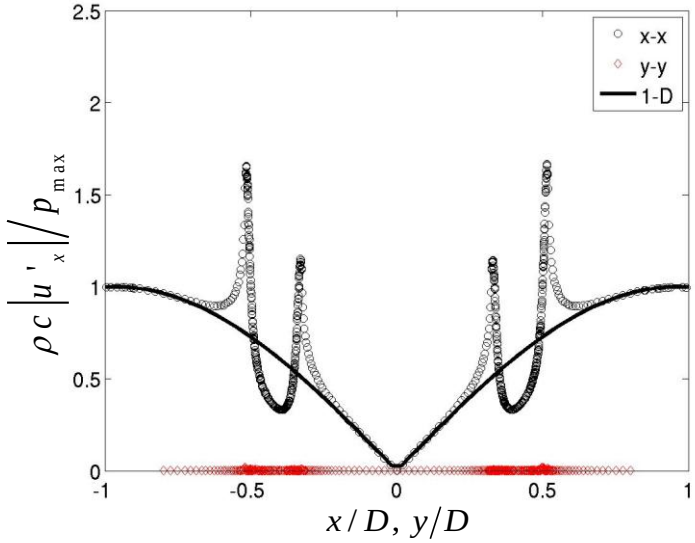

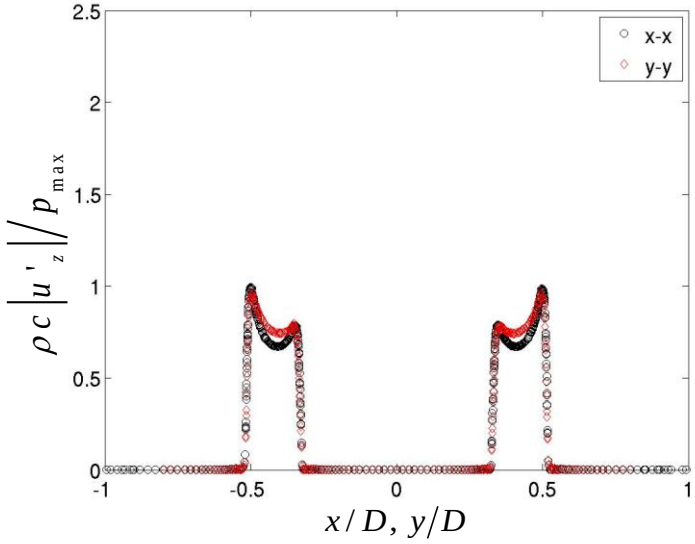

Out-of-phase, Anechoic, 2800Hz

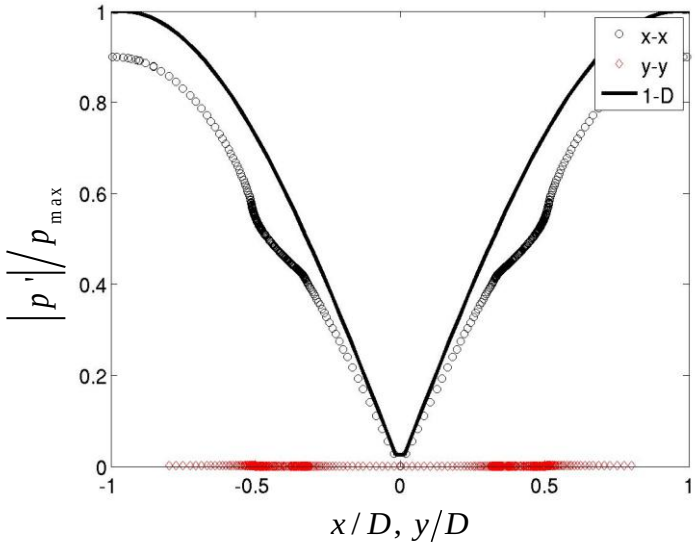

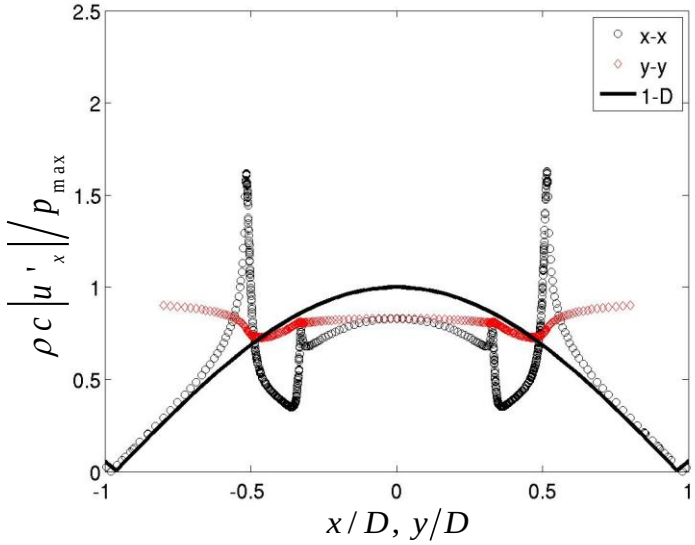

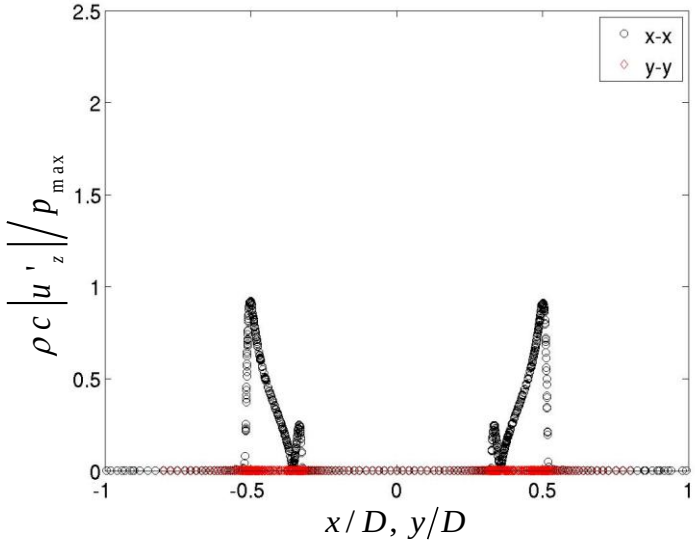

Traveling wave, Anechoic, 2800Hz

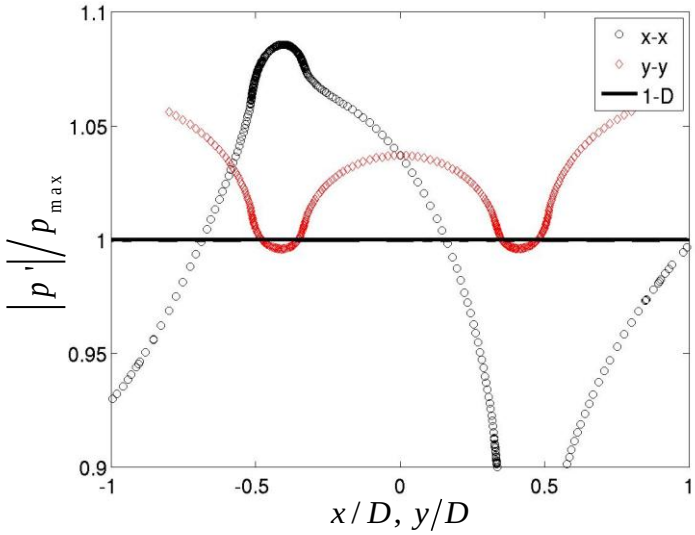

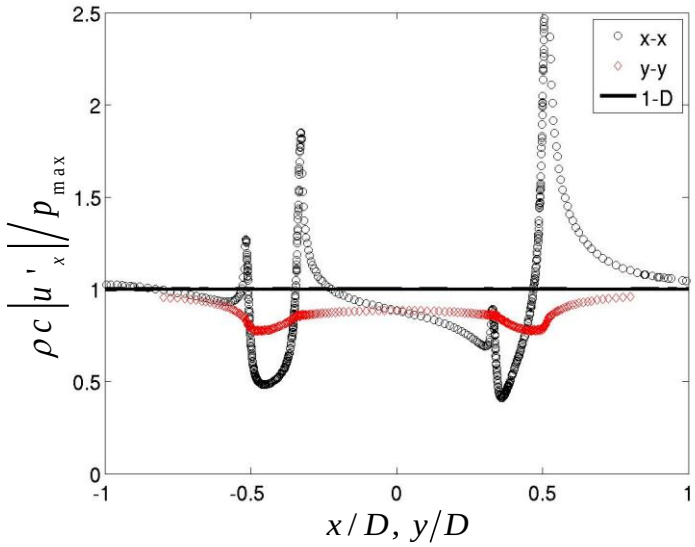

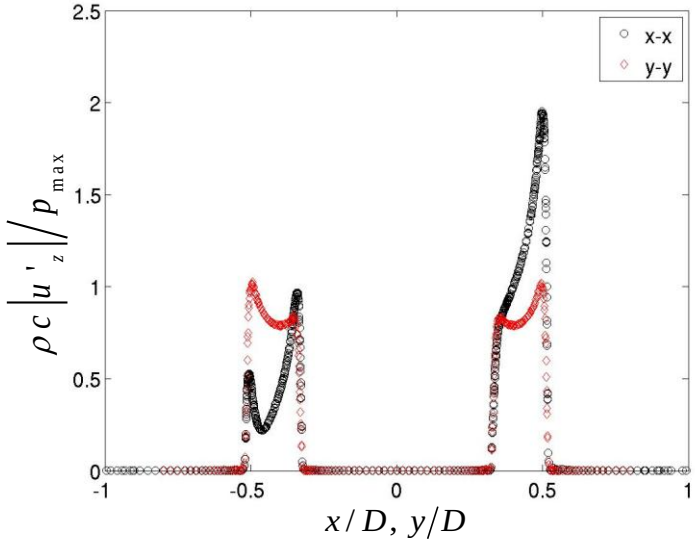

In-phase, Rigid, 1600Hz

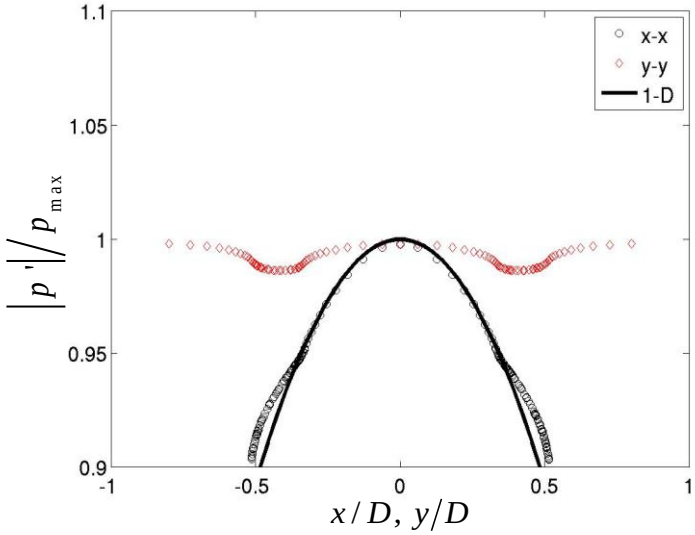

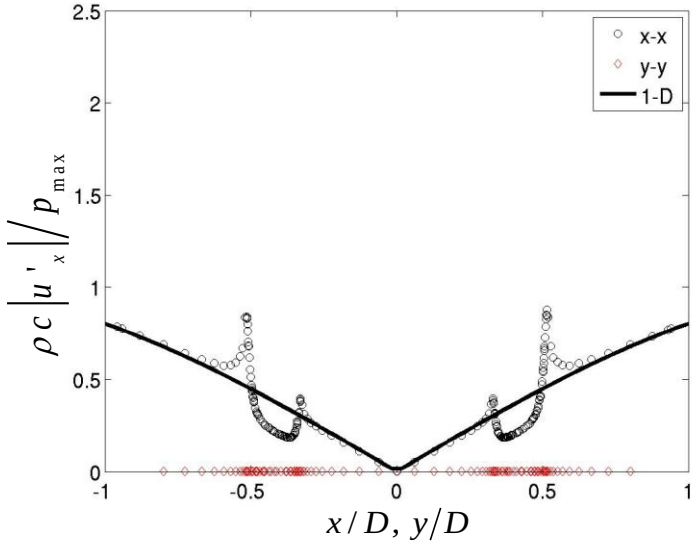

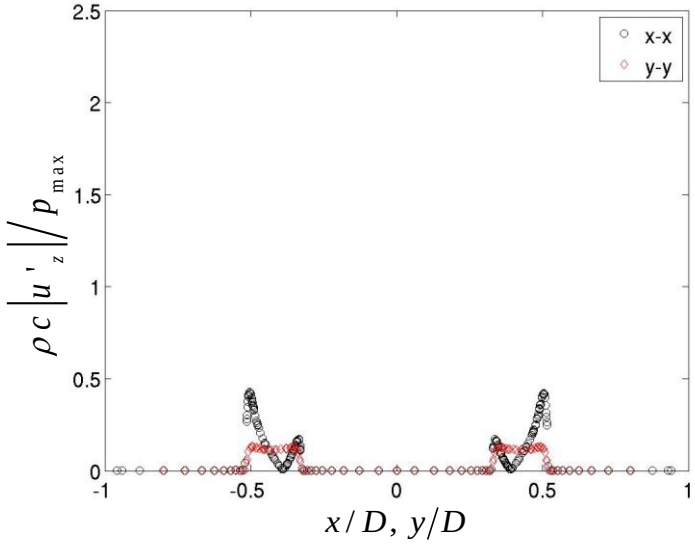

Out-of-phase, Rigid, 1600Hz

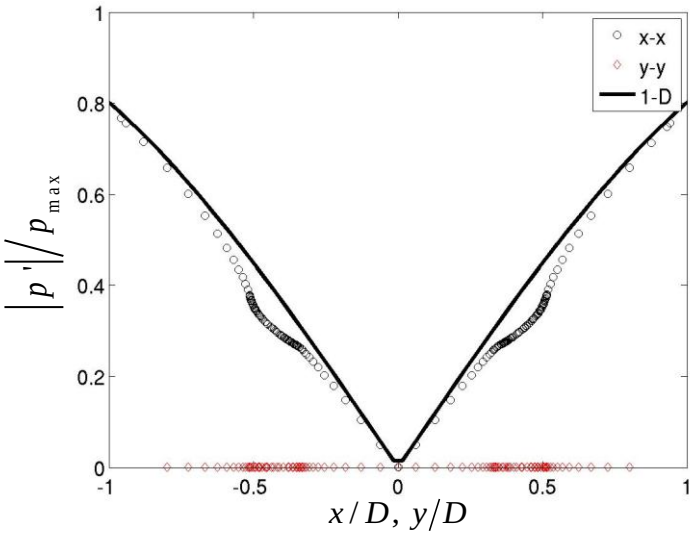

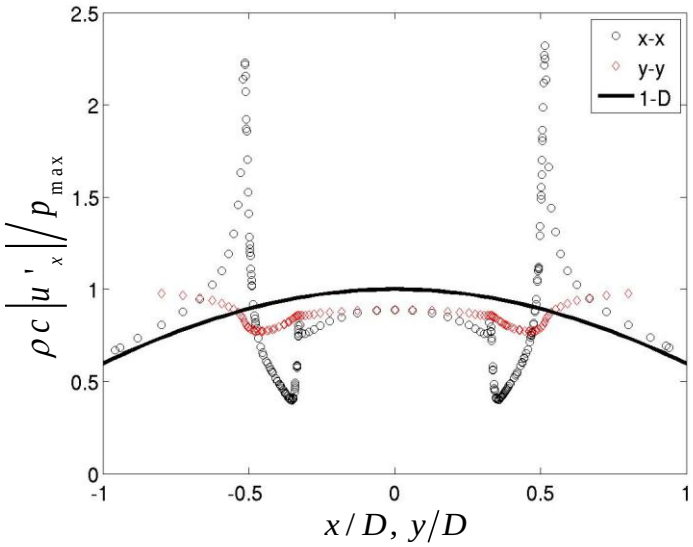

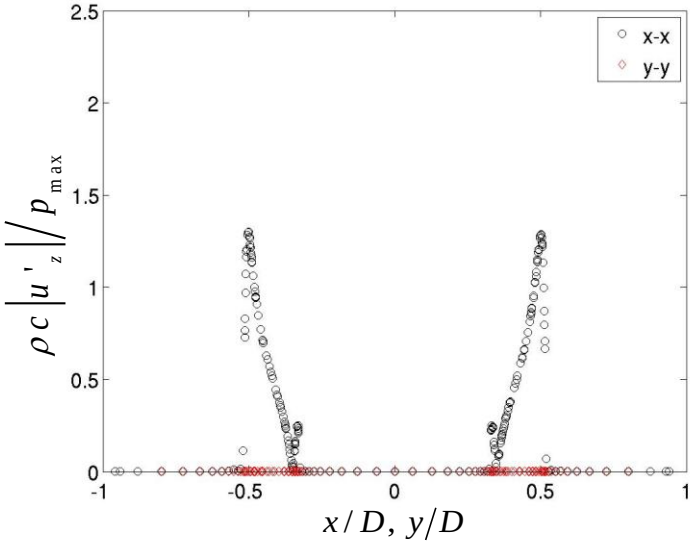

Traveling wave, Rigid, 1600Hz

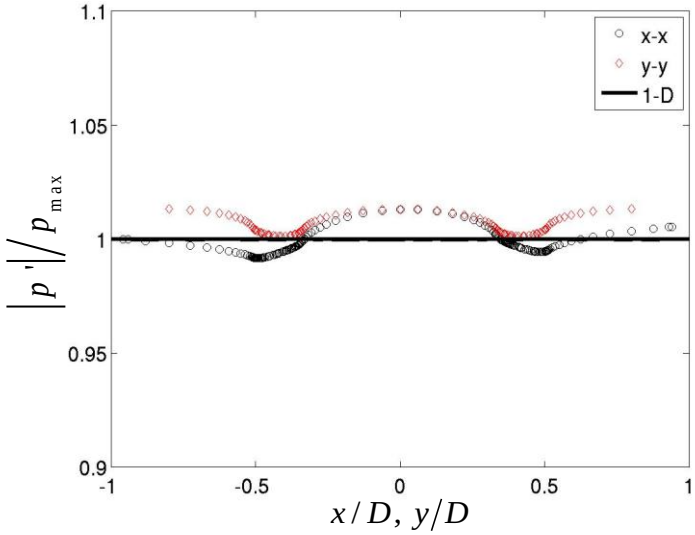

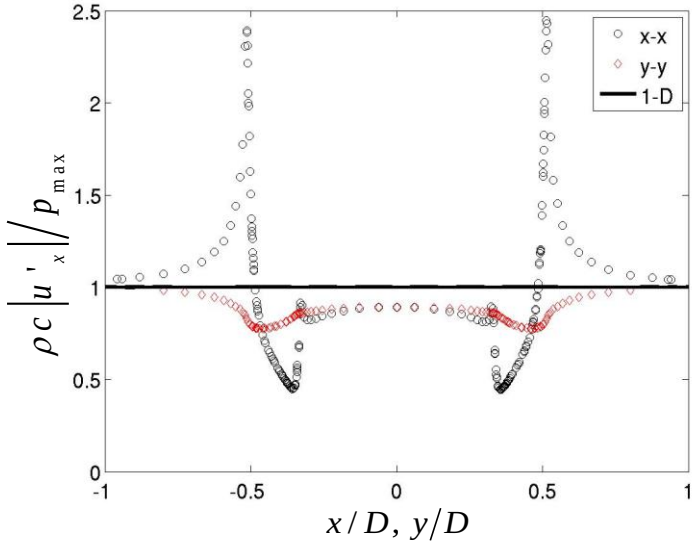

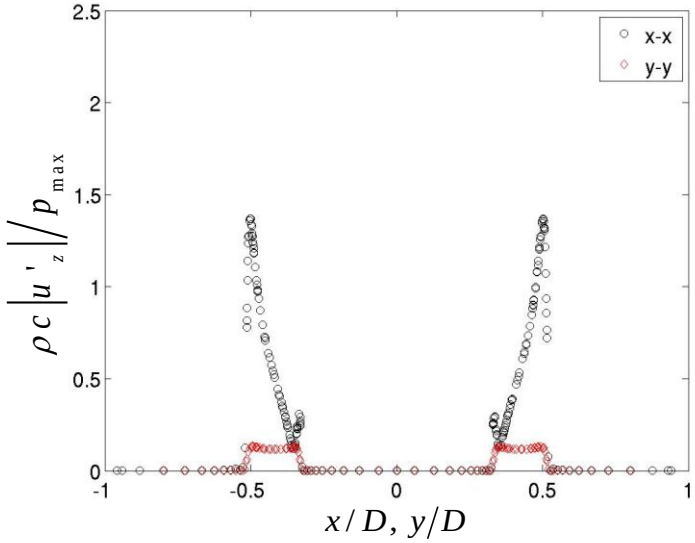

In-phase, Rigid, 2800Hz

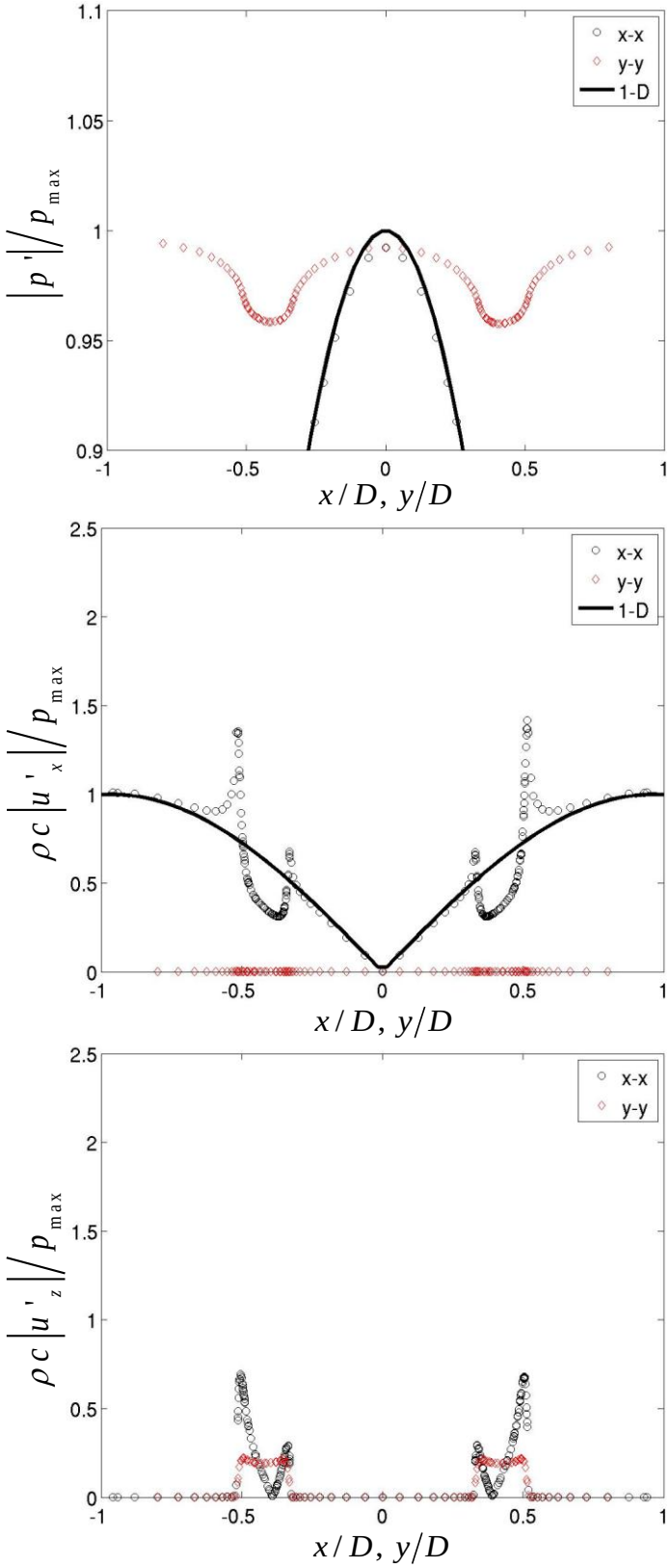

Out-of-phase, Rigid, 2800Hz

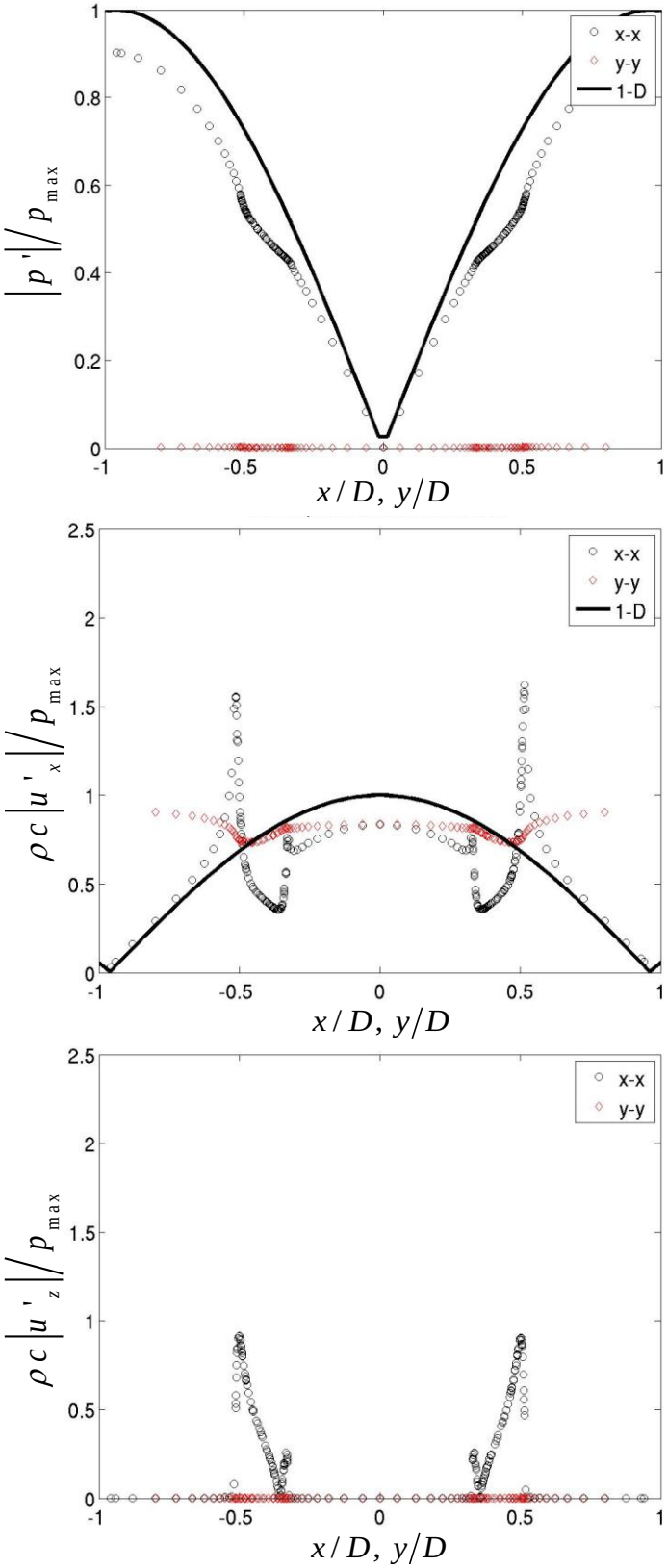

Traveling wave, Rigid, 2800Hz

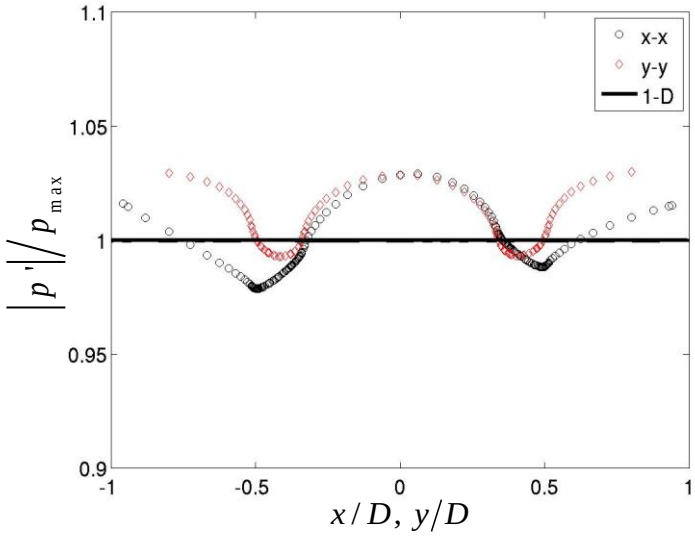

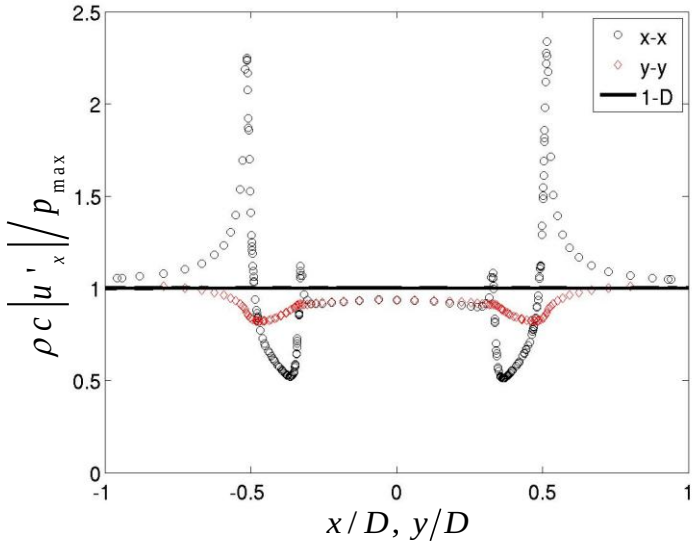

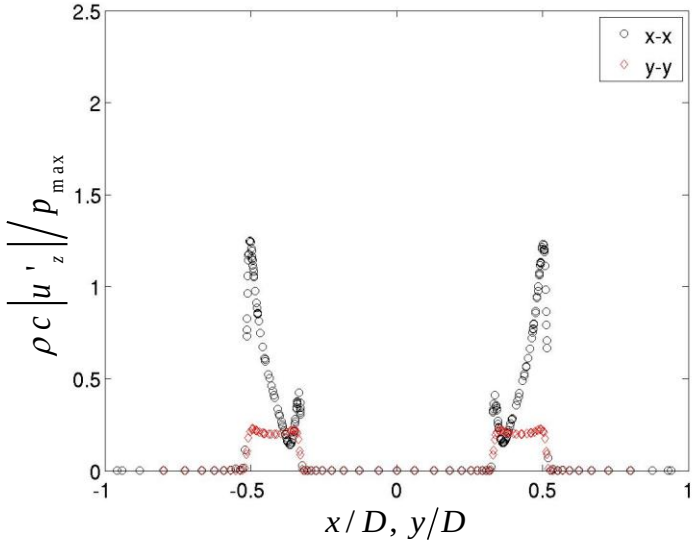

In-phase, Pressure release, 1600Hz

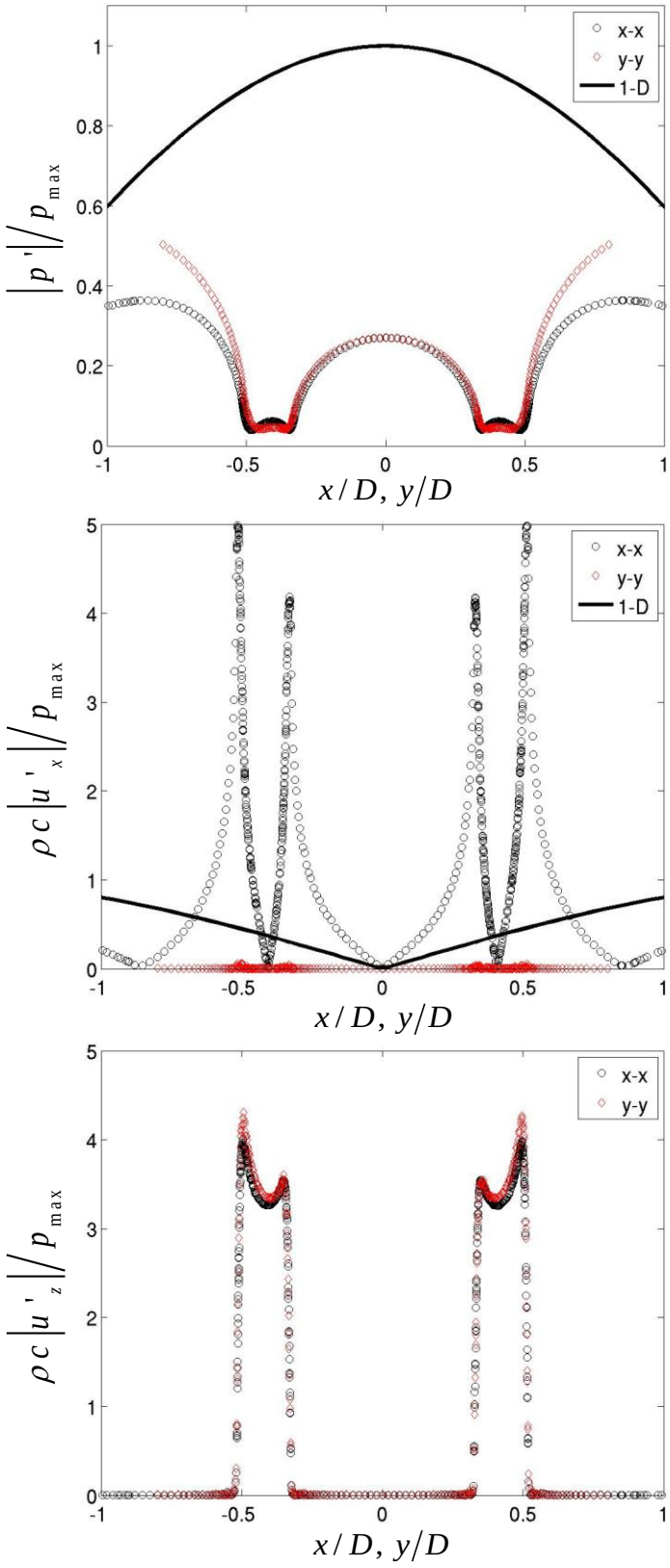

Out-of-phase, Pressure release, 1600Hz

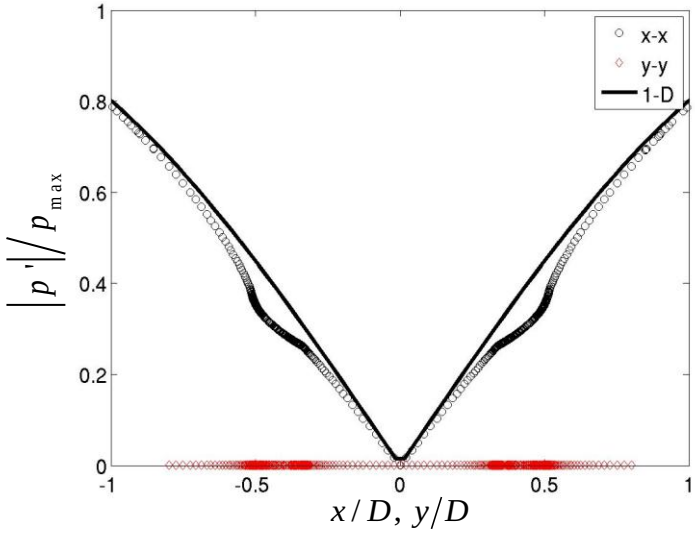

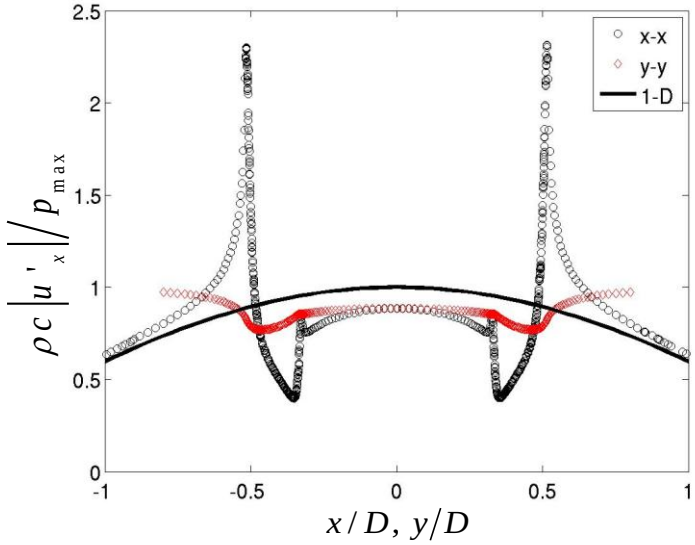

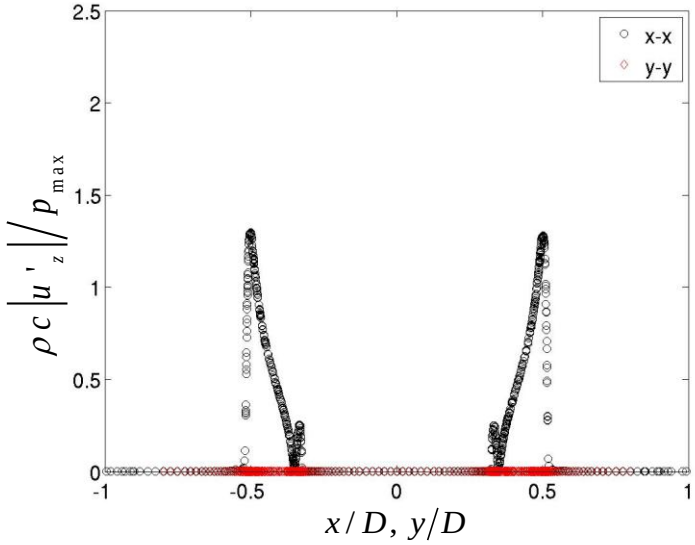

Traveling wave, Pressure release, 1600Hz

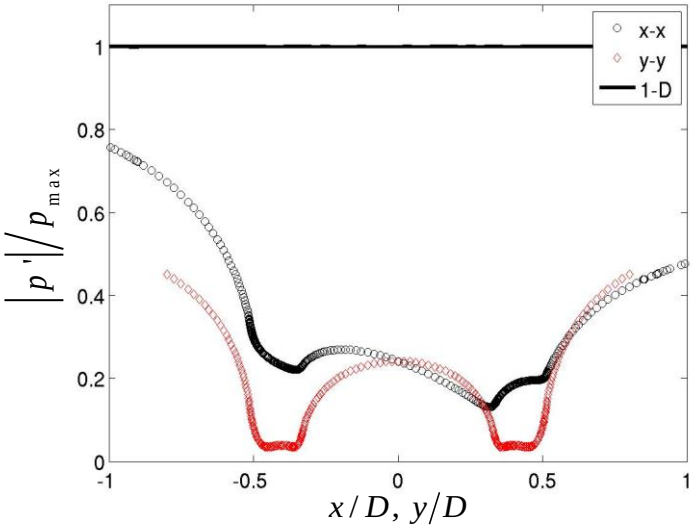

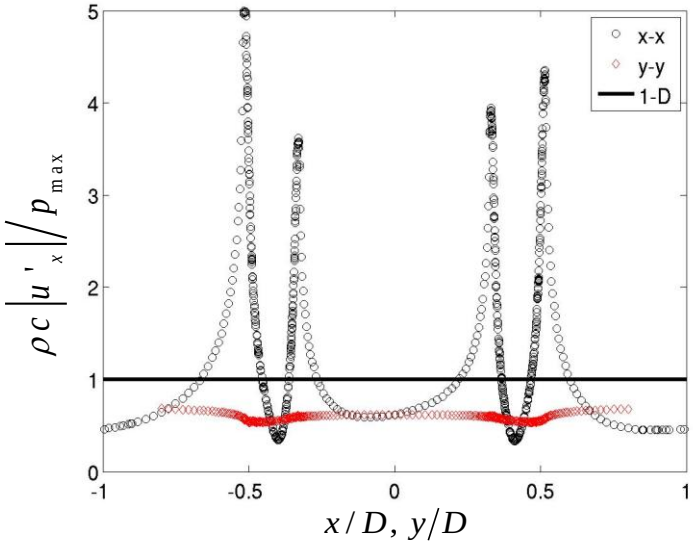

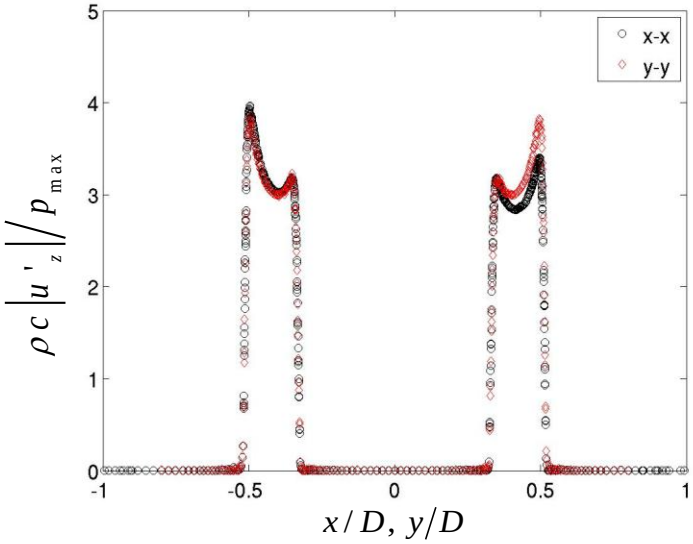

In phase, Pressure release, 2800Hz

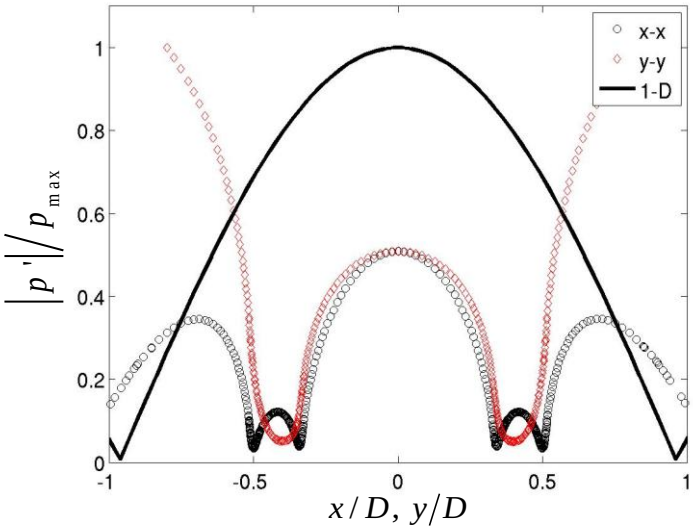

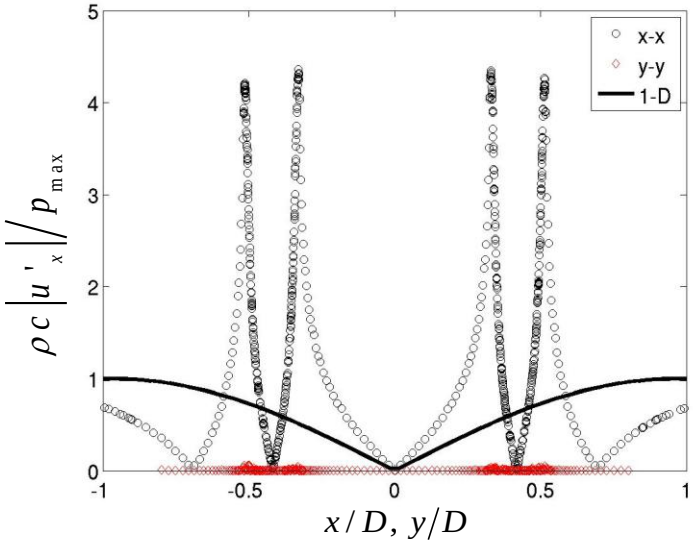

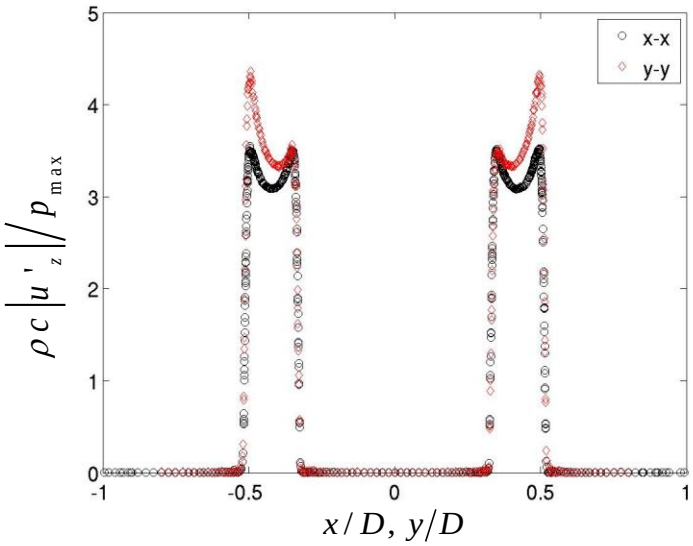

Out of phase, Pressure release, 2800Hz

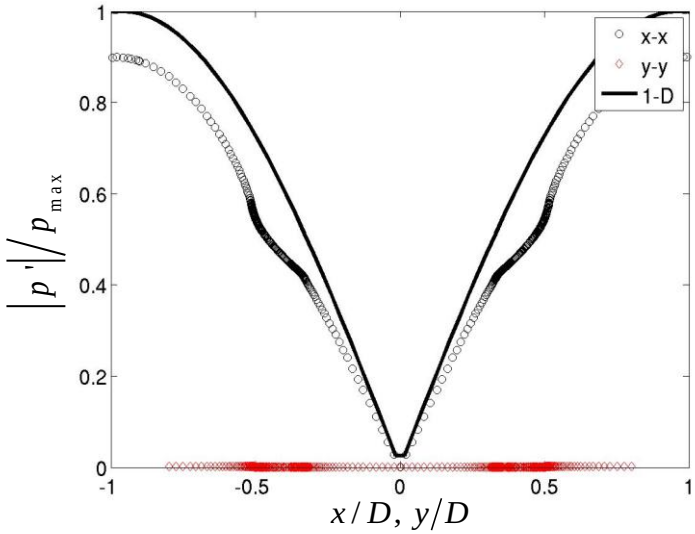

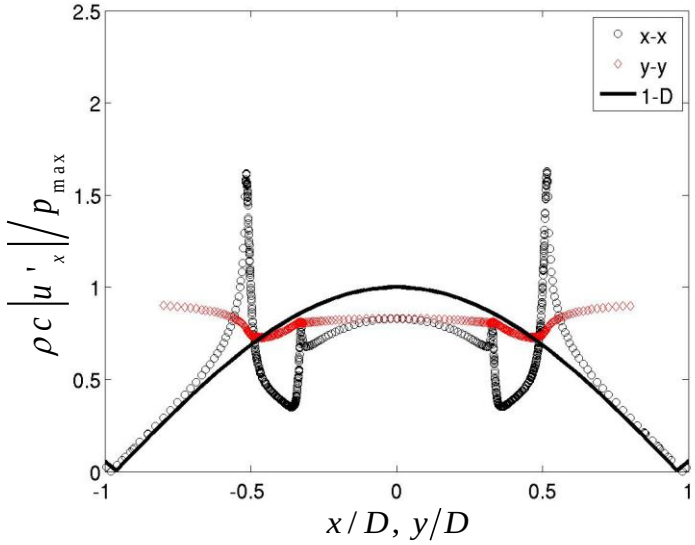

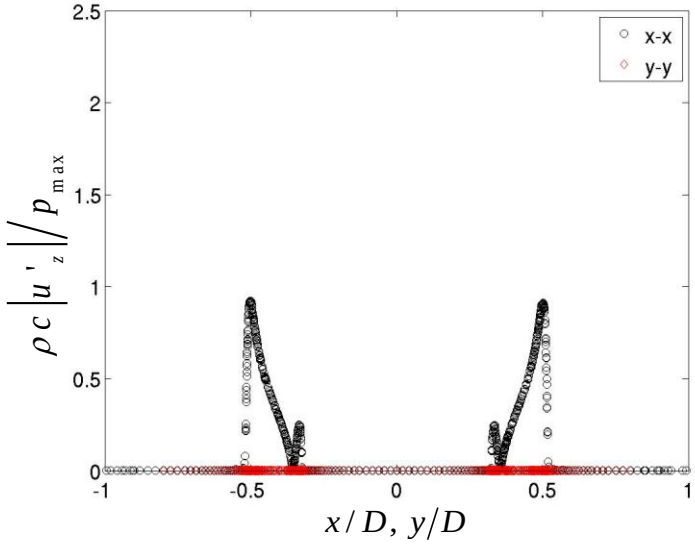

Traveling wave, Pressure release, 2800Hz

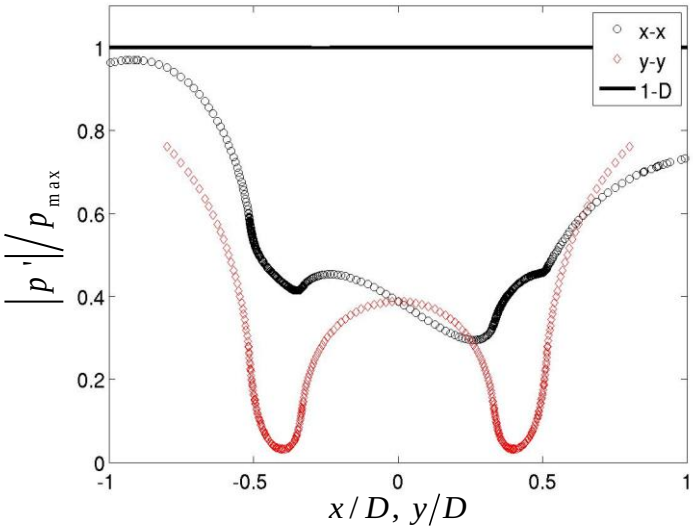

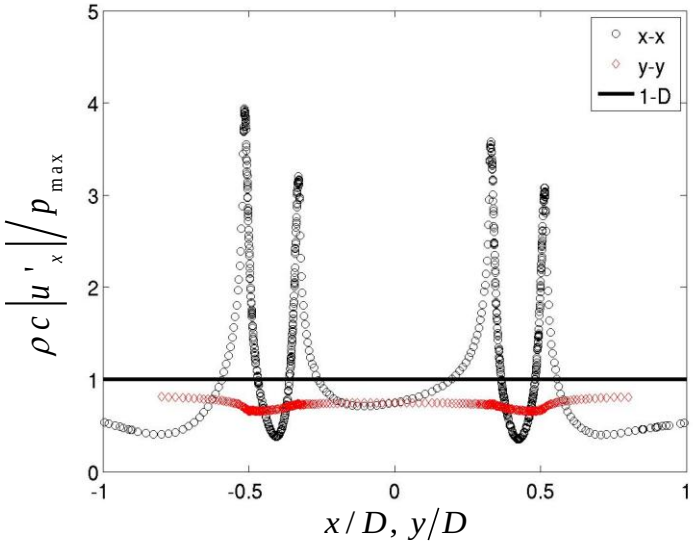

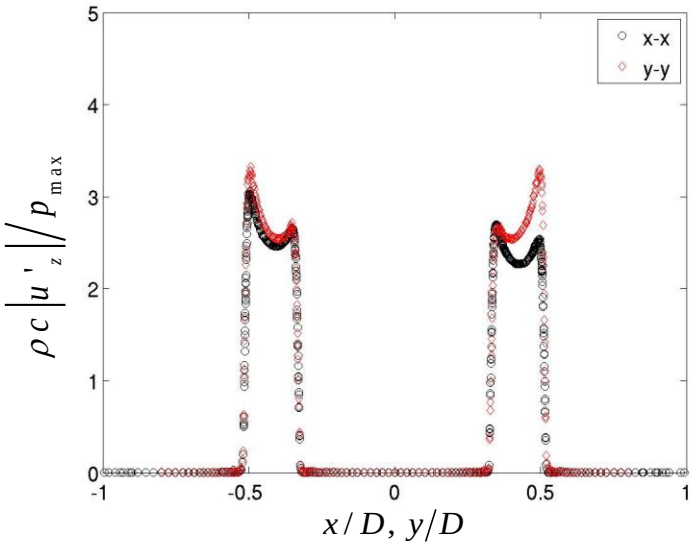

APPENDIX B

TRAVELING WAVE IMPEDANCE RATIO DATA

Table 1: Extracted data for R_Z radius dependency study mentioned in Chapter 4, for a traveling wave at 400 Hz and anechoic nozzle impedance.

Mesh #	Tolerance	Radius *(R/D)*	# Mesh Points on Radius	Wave Direction	Maximum R_Z	Axial Location *(z/D)*
1	1.00E-06	0.02	6	right	27.9367	-0.0373
	1.00E-06	0.03	6	right	18.8983	-0.0498
	1.00E-06	0.04	6	right	20.9851	-0.0523
	1.00E-06	0.05	6	right	42.1447	-0.0500
2	1.00E-06	0.025	6	right	60.3415	-0.0417
	1.00E-06	0.03	6	right	23.2985	-0.0400
	1.00E-06	0.035	6	right	56.5033	-0.0467
	1.00E-06	0.04	6	right	18.2824	-0.0533
	1.00E-06	0.045	6	right	18.1086	-0.0450
	1.00E-06	0.05	6	right	42.0193	-0.0500
	1.00E-06	0.025	6	left	60.9149	-0.0417
	1.00E-06	0.03	6	left	24.1287	-0.0400
	1.00E-06	0.035	6	left	53.9845	-0.0467
	1.00E-06	0.04	6	left	20.6833	-0.0533
	1.00E-06	0.045	6	left	18.7878	-0.0450
	1.00E-06	0.05	6	left	49.2965	-0.0500
1	1.00E-06	0.1	9	right	94.7448	-0.0647
	1.00E-06	0.2	9	right	11.5717	-0.0985
	1.00E-06	0.3	9	right	7.7402	-0.1289
	1.00E-06	0.1	9	left	62.0147	-0.0647
	1.00E-06	0.2	9	left	12.7041	-0.0985
	1.00E-06	0.3	9	left	8.0552	-0.1296
3	1.00E-06	0.01	5	right	31.7377	-0.0349
	1.00E-06	0.02	6	right	28.5792	-0.0372
	1.00E-06	0.03	8	right	23.6666	-0.0482
	1.00E-06	0.04	9	right	52.7460	-0.0487
	1.00E-06	0.05	10	right	43.3263	-0.0500

Table 1, continued

Mesh #	Tolerance	Radius *(R/D)*	# Mesh Points on Radius	Wave Direction	Maximum R_Z	Axial Location *(z/D)*
3	1.00E-06	0.01	5	left	31.3665	-0.0349
	1.00E-06	0.02	6	left	28.4243	-0.0372
	1.00E-06	0.03	8	left	25.3203	-0.0482
	1.00E-06	0.04	9	left	54.5027	-0.0487
	1.00E-06	0.05	10	left	51.0084	-0.0500
	1.00E-03	0.02	6	right	27.9367	-0.0373
	1.00E-04	0.02	6	right	27.9367	-0.0373
	1.00E-05	0.02	6	right	27.9367	-0.0373
	1.00E-06	0.02	6	right	27.9367	-0.0373
	1.00E-07	0.02	6	right	27.9367	-0.0373

REFERENCES

1. Lieuwen, T.C. and V. Yang, *Combustion Instabilities in Gas Turbine Engines, Operational Experience, Fundamental Mechanisms, and Modeling*. Progress in Astronautics and Aeronautics, ed. T.C. Lieuwen and V. Yang. 2005.
2. Rayleigh, B.J.W.S., *The Theory of Sound*. Vol. 2. 1896: Macmillan.
3. Kedia, K., S. Nagaraja, and R. Sujith, *Impact of Linear Coupling on Thermoacoustic Instabilities.* Combustion Science and Technology, 2008. **180**(9): p. 1588-1612.
4. Ducruix, S., T. Schuller, D. Durox, and S. Candel, *Combustion Dynamics and Instabilities: Elementary Coupling and Driving Mechanisms.* Journal of Propulsion and Power, 2003. **19**(5): p. 722-734.
5. Venkataraman, K., L. Preston, D. Simons, B. Lee, J. Lee, and D. Santavicca, *Mechanism of Combustion Instability in a Lean Premixed Dump Combustor.* Journal of Propulsion and Power, 1999. **15**(6): p. 909-918.
6. Palies, P., D. Durox, T. Schuller, and S. Candel, *The Combined Dynamics of Swirler and Turbulent Premixed Swirling Flames.* Combustion and Flame, 2010. **157**(9): p. 1698-1717.
7. Hirsch, C., D. Fanaca, P. Reddy, W. Polifke, and T. Sattelmayer, *Influence of the Swirler Design on the Flame Transfer Function of Premixed Flames.* Volume 2 Turbo Expo 2005, 2005: p. 151-160.
8. Paschereit, C.O., E. Gutmark, and W. Weisenstein, *Excitation of Thermoacoustic Instabilities by Interaction of Acoustics and Unstable Swirling Flow.* AIAA journal, 2000. **38**(6): p. 1025-1034.
9. Culick, F. and V. Yang, *Prediction of the Stability of Unsteady Motions in Solid-Propellant Rocket Motors.* 1992.
10. Harrje, D.T. and F.H. Reardon, *Liquid Propellant Rocket Combustion Instability*. 1972: Scientific and Technical Information Office, National Aeronautics and Space Administration.
11. Price, E.W., *Solid Rocket Combustion Instibility - An American Historical Account*, in *Nonsteady Burning and Combustion Stability of Solid Propellants*. 1992. p. 1-16.
12. Chehroudi, B., D. Talley, J.I. Rodriguez, and I.A. Leyva, *Effects of a Variable-Phase Transverse Acoustic Field on a Coaxial Injector at Subcritical and Near-Critical Conditions*, in *47th Aerospace Sciences Meeting*2008: Orlando, FL.
13. Rogers, D.E. and F.E. Marble, *A Mechanism for High-Frequency Oscillation in Ramjet Combustors and Afterburners.* Jet Propulsion, 1956. **26**(6): p. 456-464.
14. Kaskan, W.E. and A.E. Noreen, *High-Frequency Oscillations of a Flame Held by a Bluff Body.* ASME Transactions, 1955. **77**(6): p. 855-891.
15. Elias, I., *Acoustical Resonances Produced by Combustion of a Fuel-Air Mixture in a Rectangular Duct.* Journal of the Acoustical Society of America, 1959. **31**(3): p. 296-304.
16. Smith, K., L. Angello, and F. Kurzynske, *Design and Testing of an Ultra-Low NO/Sub x/Gas Turbine Combustor*, 1986, Solar Turbines Inc., San Diego, CA.

17. Krebs, W., S. Bethke, J. Lepers, P. Flohr, and B. Prade, *Thermoacoustic Design Tools and Passive Control: Siemens Power Generation Approaches*, in *Combustion Instabilities in Gas Turbine Engines*, T.C. Lieuwen and V. Yang, Editors. 2005, AIAA: Washington D.C. p. 89-112.
18. Dowling, A.P. and S.R. Stow, *Acoustic Analysis of Gas Turbine Combustors.* Journal of Propulsion and Power, 2003. **19**(5): p. 751-764.
19. Sewell, J. and P. Sobieski, *Monitoring of Combustion Instabilities: Calpine's Experience*, in *Combustion Instabilities in Gas Turbine Engines*, T.C. Lieuwen and V. Yang, Editors. 2005, AIAA: Washington D.C. p. 147-162.
20. O'Connor, J. and T. Lieuwen, *Further Characterization of the Disturbance Field in a Transversely Excited Swirl-Stabilized Flame.* Journal of Engineering for Gas Turbines and Power - Transactions of the ASME, 2012. **134**(1).
21. Cohen, J., G. Hagen, A. Banaszuk, S. Becz, and P. Mehta, *Attenuation Of Combustor Pressure Oscillations Using Symmetry Breaking*, in *49th AIAA Aerospace Sciences Meeting including the New Horizons Forum and Aerospace Exposition*2011: Orlando, Florida.
22. Hauser, M., M. Lorenz, and T. Sattelmayer. *Influence of Transversal Acoustic Excitation of the Burner Approach Flow on the Flame Structure*. in *ASME Turbo Expo*. 2010. Glasgow, Scotland.
23. O'Connor, J. and T. Lieuwen, *Disturbance Field Characteristics of a Transversely Excited Burner.* Combustion Science and Technology, 2011. **183**(5): p. 427-443.
24. Stow, S.R. and A.P. Dowling. *Low-Order Modelling of Thermoacoustic Limit Cycles*. 2004.
25. Acharya, V., Shreekrishna, D.H. Shin, and T. Lieuwen, *Swirl Effects on Harmonically Excited, Premixed Flame Kinematics.* Combustion and Flame, 2012. **159**(3): p. 1139-1150.
26. Worth, N.A. and J.R. Dawson, *Cinematographic OH-PLIF Measurements of Two Interacting Turbulent Premixed Flames with and without Acoustic Forcing.* Combustion and Flame, 2011.
27. Staffelbach, G., L.Y.M. Gicquel, G. Boudier, and T. Poinsot, *Large Eddy Simulation of Self Excited Azimuthal Modes in Annular Combustors.* Proceedings of the Combustion Institute, 2009. **32**: p. 2909-2916.
28. Wolf, P., G. Staffelbach, A. Roux, L. Gicquel, T. Poinsot, and V. Moureau, *Massively Parallel LES of Azimuthal Thermo-Acoustic Instabilities in Annular Gas Turbines.* Comptes Rendus Mecanique, 2009. **337**(6-7): p. 385-394.
29. Hutt, J.J. and M. Rocker, *High-Frequency Injection-Coupled Combustion Instability*, in *Liquid Rocket Engine Combustion Instability*, V. Yang and W.E. Anderson, Editors. 1995, American Institute of Aeronautics and Astronautics. p. 345-355.
30. Davis, D., B. Chehroudi, D. Talley, R. Engineering, and C.A. Consulting Inc Edwards Afb, *The Effects of Pressure and an Acoustic Field on a Cryogenic Coaxial Jet*, in *42nd Aerospace Sciences Meeting and Exhibit*2004: Reno, NV.
31. Camporeale, S., B. Fortunato, and G. Campa, *A Finite Element Method for Three-Dimensional Analysis of Thermo-acoustic Combustion Instability.* Journal of Engineering for Gas Turbines and Power, 2011. **133**: p. 011506.

32. O'Connor, J., J. Mannino, C.Vanatta, and T. Lieuwen, *Mechanisms for Flame Response in a Transversely Forced Flame*, in *7th US National Technical Meeting of the Combustion Institute*2011: Atlanta, GA.
33. *COMSOL Multiphysics User's Manual.* 2007.
34. Pierce, A.D., *Acoustics: An Introduction to its Physical Principles and Applications*. 1989: Acoustical Society of America.
35. Kinsler, L.E., J.V. Sanders, and A.R. Frey, *Fundamentals of Acoustics*. 3 ed. 2000: John Wiley & Sons.
36. Crighton, D.G., *The Kutta Condition in Unsteady Flow.* Annual Review of Fluid Mechanics, 1985. **17**(1): p. 411-445.